Performance considerations for expansion tube operation with a shock-heated secondary driver

David E. Gildfind[1,†], **Chris M. James**[1], **Pierpaolo Toniato**[1] **and Richard G. Morgan**[1]

[1]The Centre for Hypersonics, School of Mechanical and Mining Engineering, The University of Queensland, St Lucia, QLD 4072, Australia

A shock-heated secondary driver is a modification typically applied to an expansion tube which involves placing a volume of helium between the primary diaphragm and the test gas. This modification is normally used to either increase the driven shock strength through the test gas for high-enthalpy conditions, or to prevent transmission of primary driver flow disturbances to the test gas for low-enthalpy conditions. In comparison to the basic expansion tube, a secondary driver provides an additional configuration parameter, adds mechanical and operational complexity, and its effect on downstream flow processes is not trivial. This paper reports on a study examining operation of a shock-heated secondary driver across the entire operating envelope of a free-piston-driven expansion tube, using air as the test gas. For high-enthalpy conditions it is confirmed that the secondary driver can provide a performance increase, and it is further shown how this device can be used to fine tune the flow condition even when the free-piston driver configuration is held constant. For low-enthalpy flow conditions, wave processes through the driven tube are too closely coupled, and the secondary driver no longer significantly influences the magnitude of the final test gas flow properties. It is found that these secondary driver operating characteristics depend principally on the initial density ratio between the secondary driver helium gas and the downstream test gas.

Key words: gas dynamics, high speed flows, shock waves

1. Introduction

The secondary driver was first proposed by Henshall (1956) and evaluated experimentally by Stalker & Plumb (1968). It is normally used in expansion tubes to increase the shock strength through the test gas for high-enthalpy, superorbital conditions, and consists of an additional section of helium between the primary diaphragm and the shock tube. The theoretical principles of this mode of operation are well established (Morgan & Stalker 1991; Morgan 2001*a*); however, its effective implementation in an expansion tube is non-trivial for two reasons: firstly, the device increases the already large number of facility variables which must each be configured to achieve the desired test condition; secondly, for certain parts of

† Email address for correspondence: d.gildfind@uq.edu.au

the facility operating envelope, it can introduce complex secondary wave processes (Gildfind *et al.* 2014).

This study was motivated by recent experimentation with scramjet flow conditions using the The University of Queensland's X2 expansion tube (Gildfind *et al.* 2014). Expansion tube operation of scramjet flow conditions typically leads to a drop in sound speed across the driver/test gas interface (referred to as 'under-tailored' operation), which has been shown to promote transmission of driver disturbances to the test gas, leading to unacceptable noise levels in the final test flow (Paull & Stalker 1992). For these conditions a secondary driver has previously been suggested (Morgan & Stalker 1991) as a means to ensure that sound speed increases across this interface ('over-tailored' operation).

However, in the X2 scramjet flow condition experiments, it was found that traditional analytical techniques did not accurately predict the actual facility response for this configuration. This was attributed to close coupling of driver wave processes; however, the broader implications of this issue were not explored. The present study now examines this issue from an operational perspective, in order to establish exactly how the secondary driver affects facility response across its entire operating envelope. In doing so, the aim is to explain the unpredictable behaviour, and to develop robust guidelines for using this operating mode.

The study begins with an ideal gas analysis of a generic expansion tube across its entire practical operating envelope, using air as the test gas. A specific study of UQ's medium-sized X2 expansion tube is then performed, using equilibrium chemistry, in order compare the purely theoretical predictions with an actual facility. Numerical and experimental studies of X2 are finally used to establish which parts of the operating envelope can be accurately modelled with traditional analytical techniques, which parts require higher-fidelity numerical simulation, and the reasons for these differences are explained. Based on this wide-ranging study, general conclusions are drawn about how the response of a secondary driver changes across the entire operating envelope of an expansion tube facility, thereby providing a comprehensive and unambiguous guide to its effective implementation for expansion tubes in general.

2. Free-piston-driven expansion tubes

Free-piston-driven expansion tubes can produce the highest enthalpy and highest total pressure test flows of any type of wind tunnel test facility currently in operation. This potential has already been widely utilised for simulation of superorbital planetary entry flows up to 20 km s^{-1} (for example, Morgan & Stalker 1991; Neely & Morgan 1994; Jacobs 2011; Capra & Morgan 2012; Eichmann 2012; Porat *et al.* 2013; Sheikh *et al.* 2013; James *et al.* 2014), and their multi-gigapascal total pressure capability also makes these facilities uniquely capable of simulating the high-Mach-number flight conditions associated with scramjet access-to-space (McGilvray, Morgan & Jacobs 2010; Gildfind, Sancho & Morgan 2013; Gildfind *et al.* 2014). Both applications provide the context for this current paper.

Figure 1 shows the configuration of a basic free-piston-driven expansion tube, along with an idealised *x–t* diagram of the flow processes which occur during its operation. Compressed air from a high-pressure reservoir accelerates a massive piston down the driver/compression tube, which is sealed from the driven tube by a steel primary diaphragm. Between the piston and the diaphragm is a light driver gas such as helium, or a mixture of helium and argon. The piston accelerates across most of its stroke, reaching speeds of between 100 and 300 m s^{-1}, and accumulates significant kinetic
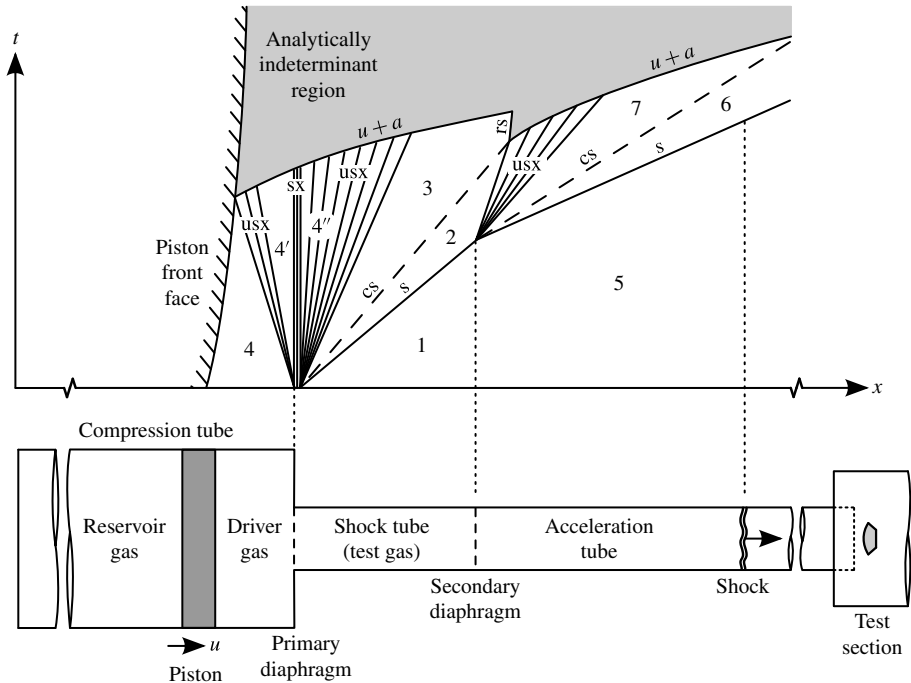
FIGURE 1. Idealised distance–time (x–t) diagram showing flow processes for a basic expansion tube: s = shock; rs = reflected shock; cs = contact surface; sx = steady expansion; usx = unsteady expansion; $u + a$ = reflected characteristic.

energy. Towards the end of the piston stroke, the driver gas compression ratio begins to rise rapidly. The piston transfers its kinetic energy to the driver gas, increasing the driver gas pressure and temperature until the steel diaphragm ruptures, whereupon the driver gas expands into the driven tube.

The driven tube has a smaller diameter and runs continuously from the primary diaphragm through to the test section. This tube can be partitioned into a series of shorter sections using thin (typically) Mylar film diaphragms. Each section can be operated with gases of different composition and initial fill pressure. In basic expansion tube mode, the driven tube is partitioned with a single diaphragm, referred to as the secondary diaphragm in figure 1. The test gas is located between the primary and secondary diaphragms, in the section referred to as the shock tube. The section of tube downstream of the secondary diaphragm – the acceleration tube – runs through to the test section, and is initially at very low pressure. Experiments take place at the exit of this tube.

The driver gas pressure and temperature are, respectively, tens of megapascals and thousands of Kelvin when the primary diaphragm ruptures. The expanding driver gas drives a strong shock through the test gas, compressing it and accelerating it towards the test section. When the hot and high-pressure test gas impacts the thin secondary diaphragm, its speed is typically between 1 and 6 km s^{-1}. The secondary diaphragm disintegrates, exposing the test gas to the low pressure (of the order of 10^0–10^2 Pa) of the downstream acceleration tube. This sudden drop in pressure causes the test gas to undergo a strong unsteady expansion, accelerating it to the final test flow velocity.

When a supersonic flow undergoes an unsteady expansion, both its total pressure and total temperature increase. Since the test gas is not stagnated during this process, expansion tubes do not suffer from the total pressure and temperature limits of facilities which do stagnate the test gas, such as reflected shock tunnels (RSTs) (Bakos & Erdos 1995), and dissociation and radiative losses are similarly avoided (Bakos, Morgan & Tamagno 1992; Morgan 2001*a*). However, since only part of the test gas can be expanded to the required test condition, test times are short in comparison to RST facilities of equivalent size (Morgan 2001*a*).

Inspecting regions 1, 2 and 5–7 in figure 1, when the secondary diaphragm is ruptured, the region 2 gas undergoes an unsteady expansion which is bounded by the initial fill pressure in the acceleration tube, p_5. Ignoring processes upstream of the shock tube for now, and making ideal gas assumptions, it follows that any given test flow condition (i.e. region 7) will be defined by a single pair of shock speeds through the shock and acceleration tubes, and the ratio of fill pressures p_5/p_1; the static pressure of the final test flow will then depend on the initial shock tube fill pressure, p_1. The fundamental purpose of the driver is therefore to generate a shock of the required strength, through a test gas at the required p_1. If an appropriate p_5 is set, then the test gas will expand to the required condition. These general trends are qualitatively observed even when real gas effects become important.

In practice, many other aspects of the facility configuration also affect the eventual performance which can be achieved. For example, the effect of boundary layers on the core flow size and final test flow velocity, which was first characterised by Duff (1959) and later quantified by Mirels (1963*a,b*), is more significant for relatively slender tubes and lower density gases. The effective 'holding time' of the free-piston driver – i.e. the amount of time at which driver pressure is held at relatively high levels – can also significantly impact test flow properties if it is insufficient (Gildfind *et al.* 2011). However, while factors such as these can potentially impose significant limitations on the performance of a facility, they are secondary in nature and can often be accounted for with careful tuning of the given facility at hand. On the other hand, the factor which most affects the fundamental performance of a facility is the state of the driver gas – in terms of sound speed and pressure – when the primary diaphragm ruptures.

2.1. *Expansion tube driver requirements*

Morgan & Stalker (1991) and Morgan (2001*a,b*) have extensively investigated the driver requirements for shock tunnel and expansion tube operation, particularly for expansion tubes operating at superorbital flight conditions. Referring to figure 1, and noting that across the interface the speed of the expanded driver gas, u_3, equals the post-shock test gas velocity, u_2, Morgan (2001*b*) normalised this velocity by the unexpanded driver gas sound speed, a_4:

$$Ma_3^* = u_3/a_4. \tag{2.1}$$

Ma_3^* is termed the 'driver equivalent Mach number' (Morgan 2001*b*). By using velocity instead of driven shock Mach number, and by non-dimensionalising u_3 in terms of a_4, the pressure ratio p_3/p_4 becomes independent of the driven gas composition (Morgan 2001*b*). Using a perfect gas analysis, where γ is the ratio of specific heats, Morgan arrived at the following driver relation:

$$\frac{p_3}{p_4} = \left[F_1 - Ma_3^* \frac{(\gamma_4 - 1)}{2}\right]^{2\gamma_4/(\gamma_4-1)}, \tag{2.2}$$
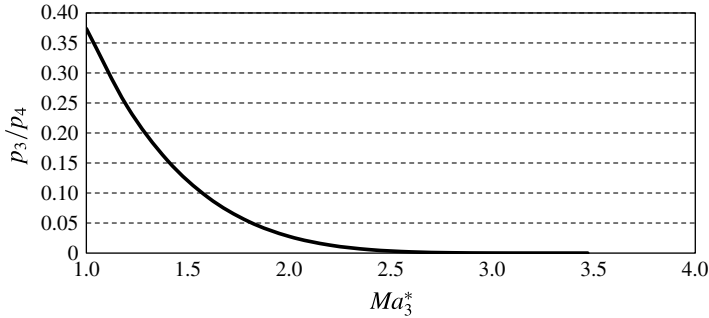
FIGURE 2. Pressure ratio required to achieve a given driver equivalent Mach number, Ma_3^*, for $Ma_{4''} = 1$ (calculated from (2.2) and (2.3)).

where:

$$F_1 = \left\{ \left[1 + \frac{\gamma_4 - 1}{2} Ma_{4''}^2 \right]^{-0.5} \left[1 + \frac{\gamma_4 - 1}{2} Ma_{4''} \right] \right\}. \tag{2.3}$$

F_1 is a parameter which accounts for the geometric transition from the driver to driven tubes. In figure 1, $Ma_{4''} = 1$; the flow is choked since there is a significant area change, and this is also the highest performance arrangement at the tube transition (Morgan 2001*b*).

Equation (2.2) indicates the extent to which the driver gas must expand, from its initial pressure, p_4, to p_3 (which is equal to the post-shock pressure, i.e. $p_3 = p_2$), to achieve a given Ma_3^*, and is plotted in figure 2. These results are for a facility with an area change at the driver, therefore $Ma_{4''} = 1$. Morgan (2001*b*) notes that the maximum possible Ma_3^* is achieved in the limiting case, when the driver gas expands to zero pressure; i.e. $p_3/p_4 = 0$. Solving for Ma_3^*:

$$Ma_3^* = 2F_1/(\gamma_4 - 1). \tag{2.4}$$

For $\gamma_4 = 5/3$ and $Ma_{4''} = 1$, equation (2.4) gives $Ma_3^* = 3.46$; for helium at room temperature (300 K) this corresponds to $u_3 = 3536$ m s^{-1}; for helium at 5000 K, which represents a free-piston driver operating at a high compression ratio, $u_3 = 11\,150$ m s^{-1}. However, observing figure 2, it can be seen that the ratio p_3/p_4 drops rapidly for $Ma_3^* > 2$; Morgan (2001*a*) notes that pressure recovery becomes too low beyond this point; the implications are test gas densities which are impractically low, and test flows which become overwhelmed by viscous effects (Mirels 1963*a*,*b*).

A practical limit of $Ma_3^* = 2$ corresponds to intermediate test gas flow velocities (region 2 in figure 1) of 2038 m s^{-1} and 6445 m s^{-1} for a helium driver at 300 K and 5000 K, respectively; this, in turn, sets a limit on final test flow velocity as well, since there are limits to the enthalpy and total pressure increases which are possible across the unsteady expansion (Morgan (2001*a*) quoting Lucasiewicz (1973) notes that up to a doubling of flow velocity can typically be achieved across an unsteady expansion). While these calculations are perfect gas estimates, they nevertheless provide an indication of the fundamental limitations of this type of driver arrangement.

2.2. *Expansion tube operation with a shock-heated secondary driver*

Figure 3 shows an idealised *x–t* diagram of the flow processes which occur for an expansion tube operating with a secondary driver. To enable this mode, a second
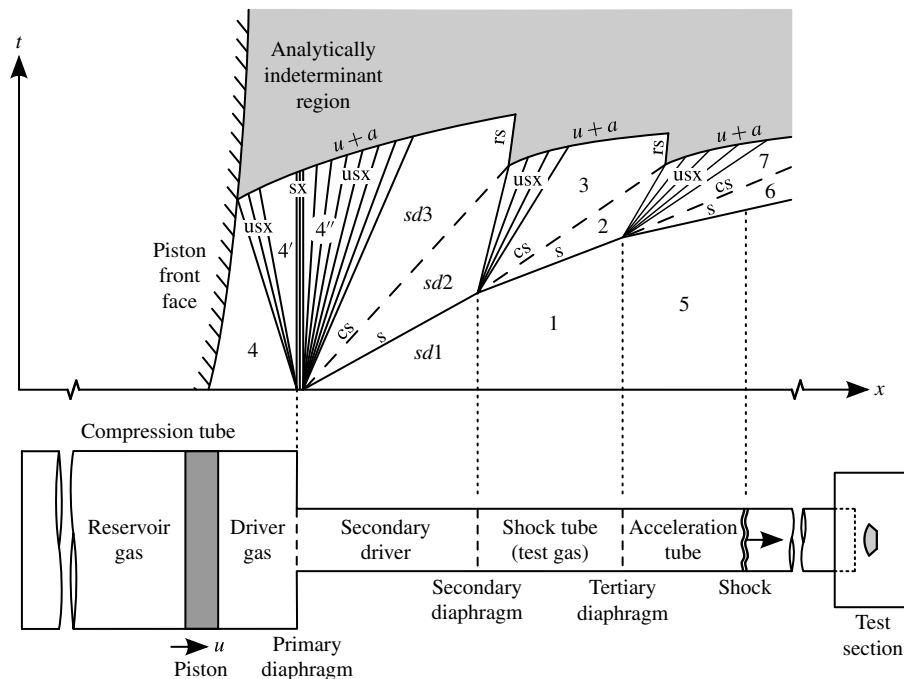
FIGURE 3. Idealised distance–time (x–t) diagram showing flow processes for an expansion tube with secondary driver and unsteady expansion at secondary diaphragm: s = shock; rs = reflected shock; cs = contact surface; sx = steady expansion; usx = unsteady expansion; $u + a$ = reflected characteristic.

thin Mylar diaphragm is used to locate a volume of helium gas between the primary diaphragm and the test gas. This is termed the secondary diaphragm; the downstream diaphragm separating the test and accelerator gases becomes the tertiary diaphragm.

This additional tube section is referred to as a secondary driver because it becomes the driver for the actual test gas (the combination of primary and secondary drivers is then referred to as a 'compound driver'). If this section of tube has a sufficiently low initial fill pressure, shock processing of its helium can raise its temperature, T_{sd2}, and therefore sound speed, a_{sd2}, far above the equivalent values of the expanded primary driver gas, T_{sd3} and a_{sd3}. When $a_{sd2} > a_{sd3}$, the secondary driver is said to be 'over-tailored'. This can result in the secondary driver generating a stronger shock through the test gas than the primary driver would be able to by itself; this performance increasing potential was the motivation for initial work with these devices, and has previously been analysed and confirmed experimentally (Henshall 1956; Stalker & Plumb 1968; Morgan & Stalker 1991; Neely & Morgan 1994; Morgan 1997, 2001*a*).

Figure 4 (from Morgan 2001*a*) compares the pressure recovery, p_3/p_4, as a function of *Ma*, for three different driver options. Taking into account practical limitations of facility operation, Morgan (2001*a*) determined that a compound driver can extend the maximum practical driver equivalent Mach number from 2 to 4. This therefore opens up the possibilities of simulating flight enthalpies to 20 000 m s^{-1} and beyond – for example, return from missions to the Far Solar System (entry to Earth's atmosphere at speeds up to 16 000 m s^{-1}), or entry to the gas giants (atmospheric entry at
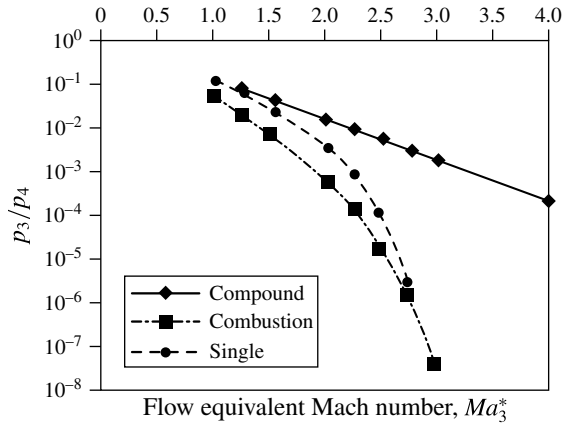
FIGURE 4. Pressure recovery, p_3/p_4, as a function of driver equivalent Mach number, Ma_3^*, for different driver options (adapted from Morgan 2001*a*).

speeds exceeding $20\,000$ m s^{-1}) – and is why this operating regime is referred to as 'superorbital' expansion tube operation. This superorbital mode was first demonstrated by Morgan & Stalker (1991), who achieved shock speeds up to 18.7 km s^{-1}; Neely & Morgan (1994) further developed the concept, with test flows up to 13 km s^{-1}.

2.3. *Secondary driver as acoustic buffer*

The first experiments with expansion tubes, which took place in the 1960s and 1970s in the United States, had in common the disappointing feature that most test flows had unacceptable levels of noise (Jones 1965; Norfleet, Lacey & Whitfield 1965; Spurk 1965; Miller 1977; Miller & Jones 1983). Miller (1977), who conducted the first extensive expansion tube study with the NASA Langley Expansion Tube/Tunnel, would later note that only a very narrow range of suitably steady test flows could be achieved (Miller & Jones 1983).

In the 1980s, The University of Queensland (UQ) was contracted by NASA Langley to investigate expansion tube operation with a free-piston driver (Stalker 1990). Paull, Stalker & Stringer (1988) undertook a systematic study with the new TQ facility to identify the reasons for the test flow unsteadiness which had been observed in the earlier expansion tube experiments. Paull & Stalker (1992) would eventually categorise test flows as being either high enthalpy or low enthalpy, and determined that test flow noise was associated with the low-enthalpy flows.

Paull & Stalker (1992) analysed the effect of the unsteady expansion on noise in the test gas, and found that the sound speed drop through the unsteady expansion had the effect of focusing the frequency components of lateral acoustic waves into a narrow bandwidth of frequencies, which would later appear as strong disturbances in the test flow. While this phenomenon was present for both high- and low-enthalpy conditions, the high-enthalpy test flows were relatively free from disturbances because the test gas had low levels of noise prior to the unsteady expansion. The critical next step was to determine that, for high-enthalpy conditions, the test gas was relatively free of noise because the sound speed of the shock-processed test gas, a_2 in figure 1, was higher than the sound speed of the expanded driver gas, a_3 (Paull & Stalker 1992).

The driver gas expansion through the driver area change and primary diaphragm is a fundamental source of lateral wave disturbances (radial disturbances in an

axisymmetric facility) (Jacobs 1994). Jacobs (1994) performed numerical simulations of the NASA Langley facility and showed that these radial disturbances could indeed propagate into the test gas. The principal conclusion from the Paull & Stalker (1992) work was that it was necessary to operate an expansion tube in an over-tailored configuration ($a_2/a_3 > 1.25$ was suggested) in order to achieve an 'acoustic buffer' against driver gas disturbances.

The acoustic buffer requirement clearly has implications for expansion tube operation at lower enthalpies; Morgan (2001a) determined that operating a basic expansion tube with $a_2/a_3 > 1.25$ would require $Ma_3^* > 1.4$. While it becomes possible to use alternative facilities, such as RSTs, to simulate these low-enthalpy test flows, there are some applications where the total pressure requirement far exceeds what other facilities can deliver. For example, high-Mach-number scramjet test flows (3–5 km s^{-1}) can have gigapascal total pressure requirements (Gildfind *et al.* 2014); however, RSTs are structurally limited to total pressures of between 150 and 300 MPa (Bakos & Erdos 1995).

Noting that over-tailored operation is a fundamental aspect of secondary driver operation, Morgan & Stalker (1991) proposed that for low-enthalpy conditions the acoustic buffer function could be met with the secondary driver, thereby, in theory, restoring the useful operational envelope of expansion tubes back to the initial predictions of Trimpi (1962). Thus, these initial years of expansion tube research at UQ led to the discovery of the mechanism responsible for the disappointingly noisy test flows in earlier studies (Paull *et al.* 1988; Paull & Stalker 1992), furthermore, the shock-heated secondary driver was introduced as a means to boost performance at superorbital conditions, and was simultaneously identified as a solution to the test flow noise problem (Morgan & Stalker 1991; Morgan 2001a).

3. Theoretical performance of an expansion tube with secondary driver

As noted in §2, there are two fundamental processes associated with producing an expansion tube test flow. Firstly, a test gas of defined composition and initial fill pressure, p_1, must be shock-processed to the required intermediate speed, u_2, and temperature, T_2. Secondly, a low acceleration tube fill pressure, p_5, is selected which will bound the unsteady expansion so that the shock-processed test gas expands to the required test flow velocity, u_7, temperature, T_7, and corresponding pressure, p_7. The performance of an expansion tube driver can be assessed during the first stage alone; i.e. measured in terms of the strength of shock which it can generate through the test gas.

In this section the influence of a secondary driver on expansion tube performance is thus assessed in terms of the pressure ratio which is achieved across the test gas shock, i.e. p_2/p_1. The purpose is not simply to determine the region of maximum performance gain, but to obtain an understanding of how the secondary driver influences performance across the entire facility operating envelope. This becomes important when a secondary driver is used as an acoustic buffer for low-enthalpy flow conditions, since this changes its mode of operation in comparison to superorbital configurations.

Ideal gas properties are assumed, which allows the facility operating envelope to be defined in terms of two initial fill pressure ratios:

(*a*) The ratio between primary driver gas pressure at diaphragm rupture and test gas fill pressure, p_4/p_1.

(*b*) The ratio between secondary driver and test gas fill pressures, p_{sd1}/p_1.

The ratio p_4/p_1 can also be used to calculate the test gas shock strength when a secondary driver is not used, and therefore provides a basis for comparison.

In this analysis the test gas is assumed to be air, and the primary and secondary driver gases are assumed to be helium. All gases are assumed to be at an initial temperature of 300 K; the primary driver gas then undergoes an isentropic compression to a temperature based on the driver gas compression ratio, λ (also specified). Trimpi's (1962) expansion tube analytical framework has been adapted to include an optional secondary driver. The driver is assumed to have a simple area change, which expands the driver gas to sonic conditions at the opening to the driver tube.

A requirement of the analytical solution approach is to establish a finite set of longitudinal wave processes for consideration during the solution process. Three typical expansion tube operating modes are considered, based on the preceding discussion:

(*a*) Figure 1 shows the basic expansion tube operating mode. The test gas is shock-processed, and then undergoes an unsteady expansion into the low-pressure acceleration tube when it ruptures the secondary diaphragm.

(*b*) Figure 3 shows an expansion tube with secondary driver. In this configuration the test gas is initially at low density relative to the secondary driver gas, and the shock-processed helium undergoes an unsteady expansion when it ruptures the secondary diaphragm. The shock-processed air then undergoes an unsteady expansion when it arrives at, and ruptures, the tertiary diaphragm. This is the assumed operating mode of previous secondary driver studies targeting superorbital expansion tube operation (Morgan & Stalker 1991; Neely & Morgan 1994).

(*c*) Figure 5 also shows an expansion tube with secondary driver. The difference compared to figure 3 is that the test gas initially has sufficiently high density, compared to the secondary driver gas, that the shock-processed secondary driver gas must slow when it impacts the test gas. This deceleration and corresponding compression occur due to a reflected shock originating at the secondary diaphragm. The remaining downstream flow processes are otherwise similar to figure 3.

Appendix A details the steps involved in solving for the test flow properties, given an initial pair of pressure ratios, p_4/p_1 and p_{sd1}/p_1. The results of the analysis are shown in figure 6. Figure 6(*a*) shows the computed pressure ratio across the test gas shock, p_2/p_1, for an expansion tube operating both with (shaded surface) and without (white surface) a secondary driver. The driver compression ratio is $\lambda = 1$ for both solutions (i.e. no compressive heating of the driver gas).

It can be seen that the white surface plot in figure 6(*a*) is invariant with p_{sd1}/p_1 since it considers the basic expansion tube without secondary driver. However, it can be seen that the shaded plot varies significantly with this ratio. There is a clear region of operation where the secondary driver theoretically imparts a performance increase. On the log–log scale shown, this region is delineated by two approximately straight boundaries:

(*a*) The dashed black curve in figure 6(*a*) represents the tailored condition in figure 3 where the sound speed of the expanded primary driver gas, a_{sd3}, is equal to the sound speed of the shock-processed secondary driver gas, a_{sd2}. Noting (3.1), and that the primary driver sound speed, a_4, is constant for all of figure 6(*a*), then tailored operation corresponds to a single secondary driver shock speed, and
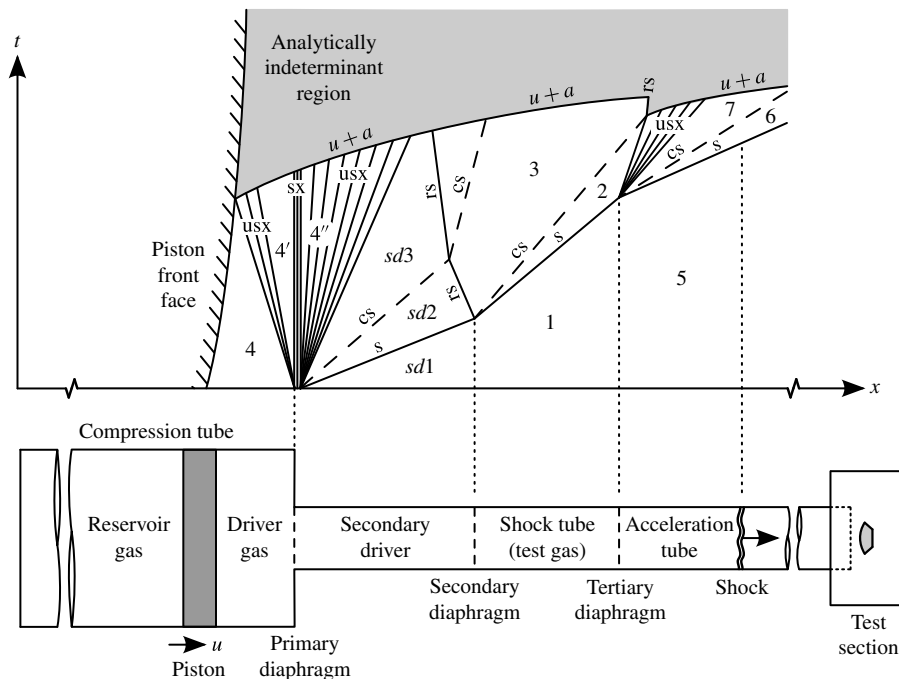
FIGURE 5. Idealised distance–time (x–t) diagram showing flow processes for an expansion tube with secondary driver and reflected shock at secondary diaphragm: s = shock; rs = reflected shock; cs = contact surface; sx = steady expansion; usx = unsteady expansion; $u + a$ = reflected characteristic.

therefore a fixed pressure ratio, p_4/p_{sd1}; this explains why the dashed curve is straight:

$$\frac{p_4}{p_{sd1}} = \frac{p_4}{p_1} \cdot \frac{p_1}{p_{sd1}}. \tag{3.1}$$

Considering each point on the dashed curve, at higher ratios of p_{sd1}/p_1 the condition $a_{sd2} > a_{sd3}$ arises, and the secondary driver is said to be 'over-tailored' with respect to the primary driver gas. This is the fundamental operating regime which allows the secondary driver gas to achieve a stronger shock than the primary driver gas alone (Morgan 2001*a*), and corresponds to a performance increase relative to the basic expansion tube. Conversely, at lower ratios of p_{sd1}/p_1 the secondary driver is under-tailored, and the performance is reduced in comparison to the basic expansion tube.

(*b*) A solid black diagonal line is shown in figure 6(*a*); this marks the beginning of the region of operation where a reflected shock forms upon rupture of the secondary diaphragm (i.e. the case shown in figure 5), and p_2/p_1 is seen to reduce compared to the basic expansion tube. For each point on the solid curve, a smaller ratio of p_{sd1}/p_1 will result in a performance reduction compared to the basic expansion tube. This operating mode is examined in more detail in § 3.1.

The shaded surface in figure 6(*b*) shows the local ratio between the two surfaces in figure 6(*a*), again for $\lambda = 1$; this has been calculated by dividing each local pressure ratio for operation with a secondary driver (from the shaded surface in figure 6(*a*), and denoted here as $p_{2,sd}$) by the corresponding pressure ratio for operation without
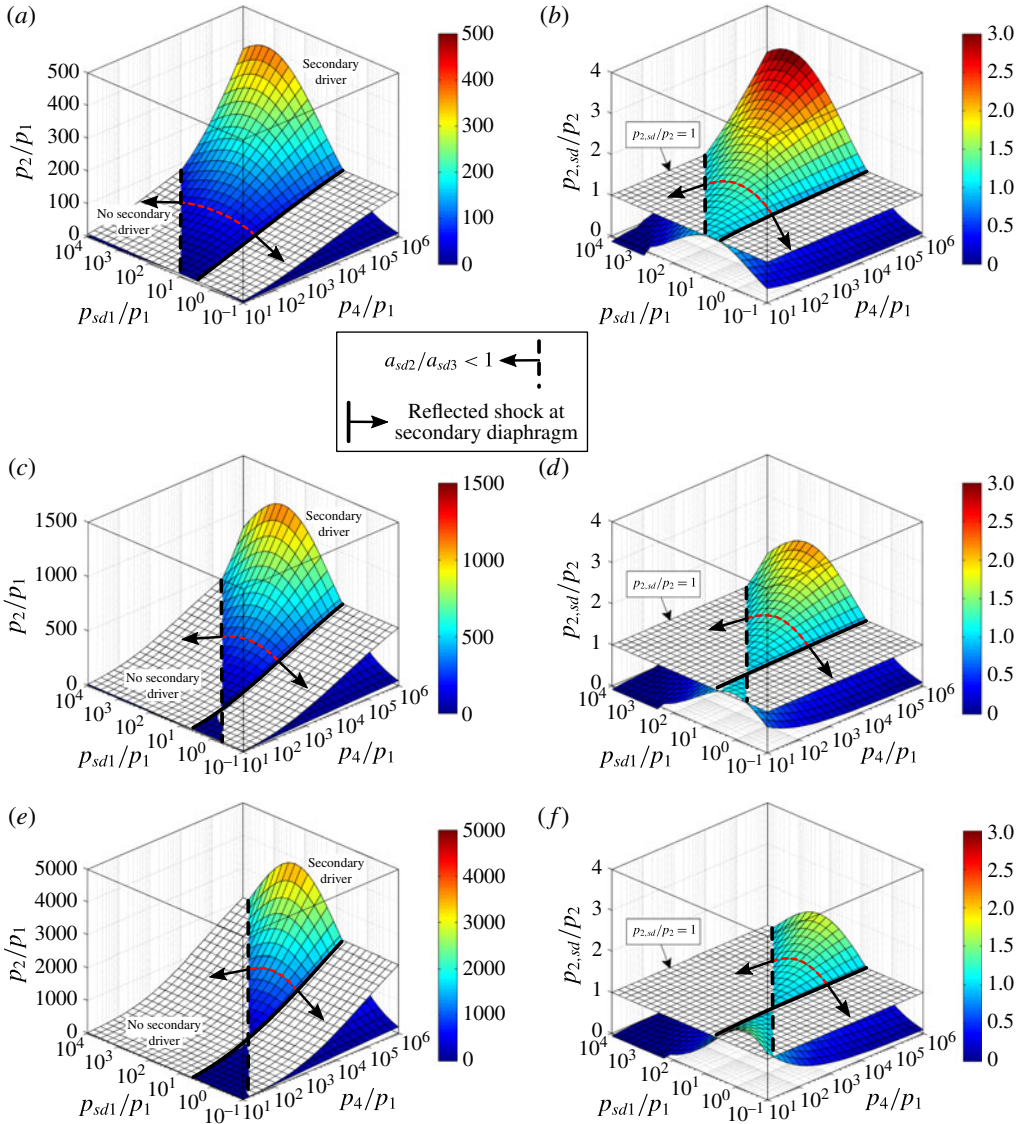
FIGURE 6. (Colour online) Influence of a helium secondary driver on pressure ratio across test gas shock wave, for air test gas and helium primary driver; (*a*), (*c*) and (*e*) show p_2/p_1, with and without secondary driver, for $\lambda = 1$, 10 and 100, respectively; (*b*), (*d*) and (*f*) show the ratio between the two shock-processed test gas pressure ratios, with and without secondary driver, also for $\lambda = 1$, 10 and 100, respectively.

a secondary driver (from the white surface in figure 6(*a*), and denoted p_2). The white surface in figure 6(*b*) shows the ratio $p_{2,sd}/p_2 = 1$; anywhere that the shaded surface exceeds this level, the secondary driver theoretically provides a performance increase. The dashed and solid curves once more delineate this region of performance increase; the dashed curve defines the boundary between over-tailored and under-tailored operation; the solid curve defines the threshold where the unsteady expansion is replaced by a reflected shock at the secondary diaphragm.

The analysis of figure 6(*a,b*) is repeated for $\lambda = 10$ and $\lambda = 100$ in 6(*c,d*) and 6(*e,f*), respectively. Considering the entire set of plots, four features are evident:

(*a*) The shapes of each surface, and the delineating dashed and solid boundaries, are all qualitatively the same.

(*b*) With increased driver compression ratio, λ, the absolute pressure ratio achieved by the driver, both with and without secondary driver, increases.

(*c*) Within the range of fill pressure ratios considered, the relative performance increase (i.e. figure 6*b,d,f*) achieved with the secondary driver diminishes with increased λ.

(*d*) There is a small region in figure 6(*c–f*) where under-tailored operation, combined with a reflected shock at the secondary diaphragm, theoretically results in a marginal increase in performance compared to the basic expansion tube (this is most evident in figure 6*f*).

3.1. *Reflected shock at the secondary diaphragm*

An important feature in figure 6 is that although the secondary driver can be configured for over-tailored operation across a large part of the performance envelope, this performance increase is lost if a reflected shock arises at the secondary diaphragm. While it will be later shown that this becomes a fundamental feature of secondary driver operation at lower enthalpies, where the device is used as an acoustic buffer, in this section the conditions to produce a reflected shock are first examined.

Whether or not a reflected shock arises at the secondary diaphragm depends primarily on the ratio of initial fill pressures in the secondary driver and shock tubes (p_{sd1} and p_1, respectively), and to a lesser extent on the strength of the resulting shock in the shock tube. For $p_1 \ll p_{sd1}$, an unsteady expansion will occur; if p_1 is increased, eventually a point will be reached where the unsteady expansion has zero strength; if p_1 is further increased, a reflected shock wave will form. The weakest reflected shock will be a Mach wave, and will produce negligible pressure rise, and negligible deceleration, of the region *sd*2 flow; for this case $u_{sd2} = u_3$ and $p_{sd2} = p_3$. If ideal gas assumptions are made, the density ratio associated with this condition, ρ_{sd1}/ρ_1, can be solved as a function of test gas shock strength, expressed in terms of Mach number $Ma_{s,1}$. Section A.3 details the procedure to solve for the reflected Mach wave case; the results are shown in figure 7.

Figure 7 shows two solutions for the reflected Mach wave case. The curve denoted 'Solution 1' is the only physical solution. It can be seen that, except for weak shocks, the ratio $\rho_{sd1}/\rho_1 \approx 0.9$ indicates the density ratio below which a reflected shock will form in the secondary driver gas. For $\rho_{sd1}/\rho_1 > 0.9$, the secondary driver gas is sufficiently dense that it will undergo an unsteady expansion into the test gas for all test gas shock speeds.

'Solution 2' in figure 7 represents the shock Mach number which the secondary driver will drive through the test gas simply by virtue of its high initial fill pressure; i.e. with no initial velocity, and independent of the upstream driver. It is a non-physical solution, since this expansion process must occur through an expansion wave, not a Mach wave. The correct solution is given by (3.2), which is the basic shock tube equation (equation (7.94) from Anderson 1990), and is the dashed curve shown in figure 7. The two solutions are coincidentally equal for $Ma_{s,1} = 1$, for which the driven shock through the test gas is a Mach wave with no associated pressure rise;
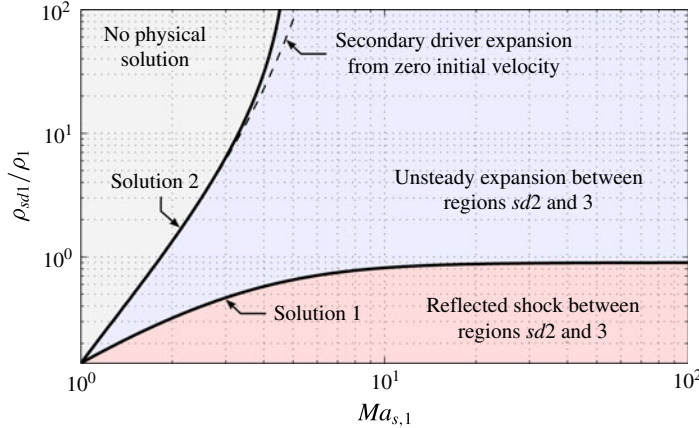
FIGURE 7. (Colour online) Effect of secondary driver/test gas fill density ratio, ρ_{sd1}/ρ_1, on post-diaphragm rupture flow processes. Secondary driver is helium; test gas is air.

the two curves diverge for $Ma_{s,1} > 1$, since only the shock tube equation is physically correct.

$$
\frac{p_{sd1}}{p_1} = \frac{p_2}{p_1} \left\{ 1 - \frac{(\gamma_{sd} - 1) \left(\dfrac{a_1}{a_{sd1}} \right) \left(\dfrac{p_2}{p_1} - 1 \right)}{\sqrt{2\gamma_1 \left[2\gamma_1 + (\gamma_1 + 1) \left(\dfrac{p_2}{p_1} - 1 \right) \right]}} \right\}^{-2\gamma_{sd}/(\gamma_{sd}-1)}. \tag{3.2}
$$

For an air test gas, the result observed in figure 7 effectively limits the use of a secondary driver as a performance increasing device to superorbital conditions only. This limitation will be less restrictive for lighter test gases.

4. X2 driver performance envelope

In this section the performance envelope of the X2 expansion tube is examined using the facility's high-performance 100 % helium tuned-driver condition. This condition is described in Gildfind, James & Morgan (2015), and summarised in table 1. A schematic of the X2 facility is shown in figure 8, and a detailed overview of the facility is provided in Gildfind *et al.* (2014). The analysis of Gildfind *et al.* (2015) determined that reasonably accurate driven shock speed estimates could be obtained analytically by assuming a constant driver temperature and pressure of $\overline{T}_4 = 2903$ K and $\overline{p}_4 = 27.4$ MPa, respectively, and treating the driver gas as ideal.

The discrepancy between analytical calculations and experimentally measured shock speeds was less than 3 % for shock speeds into a helium driver gas between approximately 4 and 9 km s^{-1}; another 5 km s^{-1} shock speed through air was predicted to within 3.6 % (using equilibrium gas assumptions for the air). Since the present analysis is focused on shock speeds through a helium secondary driver, the analytical values derived in Gildfind *et al.* (2015) are considered a good basis for such a parametric study.

Using effective driver gas properties from table 1, an iterative analytical routine was established to predict the shock speed through an air test gas for X2 expansion tube
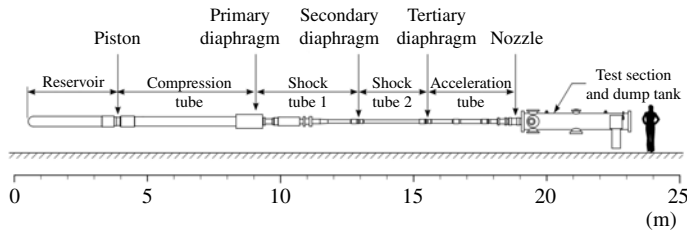
FIGURE 8. The University of Queensland's X2 expansion tube facility (to scale). Supporting carriage work, pressure manifold and associated hardware are not shown.

Driver condition I.D.	Driver gas composition	Orifice plate $\varnothing$ (mm)	Diaphragm thickness (mm)	Rupture pressure (MPa)	Reservoir fill pressure (MPa)	Driver fill pressure (kPa)
x2-lwp-2.0mm-100He-0	100 % He	65	2.0	27.9	6.85	92.8

TABLE 1. X2 10.5 kg piston-tuned driver condition, with effective $\bar{p}_4$ and $\overline{T}_4$ of 27.4 MPa and 2903 K, respectively (Gildfind *et al.* 2015); driver gas composition is by partial pressure; diaphragms are fabricated from cold rolled steel.

operation with and without a secondary driver. Flow processes were assumed to follow those shown in figures 1, 3 and 5. For this driver condition, an orifice plate is located at the driver area change; this was modelled in accordance with the methodology detailed in Gildfind *et al.* (2015). Ideal gas properties were assumed for primary driver and secondary driver helium gases; equilibrium gas properties were used for the air test gas, and were calculated using CEA (Chemical Equilibrium with Applications) (Gordon & McBride 1994). The basic methodology to calculate equilibrium shock speeds through the test gas was as follows:

(*a*) A matrix of combinations of helium secondary driver fill pressure, p_{sd1}, and air test gas fill pressure, p_1, was established. Both p_{sd1} and p_1 were varied between 10^2 and 10^6 Pa, and incremented with equal-sized steps on a log scale.

(*b*) The shock speed through the secondary driver was calculated in accordance with § A.2, providing the post-shock properties in region *sd*2 (figure 3).

(*c*) For each p_1, CEA was used to calculate post-shock flow properties through air, across shock speeds ranging from 400 to 11 000 m s^{-1}, incremented by 50 m s^{-1}, and covering the likely range of shock speeds through the test gas. These results were recorded as a look-up-table for subsequent calculations; this would then provide equilibrium curves of p_2 versus u_2 for each p_1.

(*d*) Test gas shock speeds for each p_{sd1} were calculated for both unsteady expansion (figure 3) and reflected shock (figure 5) wave processes at the secondary diaphragm. For the unsteady expansion case, the region *sd*2 gas was incrementally expanded to a pressure approaching zero, and the corresponding velocity calculated at each point; for the reflected shock case, the region *sd*2 gas was compressed by a reflected shock to a velocity approaching zero, and the corresponding pressure calculated; both calculation procedures were based on the methodology detailed in § A.2. The outputs of this calculation were curves of p_{sd2} versus u_{sd2} for both unsteady expansion and reflected shock cases.

(*e*) At the final step, for each p_1, the intersections between the equilibrium air p_2 versus u_2 curve and the two p_{sd2} versus u_{sd2} curves were calculated. The unsteady expansion solution was considered to be correct if both $p_{sd2} > p_3$ and $u_{sd2} < u_3$; otherwise the reflected shock solution was used, where $p_{sd2} < p_3$ and $u_{sd2} > u_3$. The type of solution was also recorded for each p_1.

(*f*) A similar procedure was also used to calculate the test gas shock speed for a basic expansion tube without a secondary driver. In this case, the region $4''$ driver gas undergoes an unsteady expansion to the test gas velocity in accordance with § A.1.

Figure 9(*a*) shows computed test gas shock speed, u_{s1}, for $p_1 = 10^2$–10^6 Pa, which is representative of the entire envelope of shock tube fill pressures across which this facility might be used. The white surface represents u_{s1} for a basic shock tube; this surface is invariant with the p_{sd1} axis, since this configuration does not use a secondary driver. The grey surface shows u_{s1} using a helium secondary driver, with p_{sd1} ranging from 10^2 to 10^6 Pa. Consistent with the ideal gas analysis in § 3, it is clear from the plot that there is a region of operation where the secondary driver theoretically confers a significant shock speed increase through the test gas; outside this region the presence of a secondary driver serves to theoretically reduce test gas shock speed compared to the basic configuration.

Figure 9(*b*) delineates the operating region where a secondary driver theoretically imparts a performance increase for X2. The light grey region of the surface plot indicates conditions where the secondary driver gas undergoes an unsteady expansion into the test gas (the case shown in figure 3). The line running parallel to the p_1 axis, i.e. $p_{sd1} \approx 390$ kPa, represents the tailored condition where $a_{sd3} = a_{sd2}$ (this is later shown explicitly in figure 11). At even lower p_{sd1}, i.e. $p_{sd1} < 390$ kPa, the condition $a_{sd2} > a_{sd3}$ arises, and the secondary driver is said to be 'over-tailored', and a performance increase relative to the basic expansion tube is expected.

However, a diagonal line is also observed in figure 9(*b*); this marks the boundary of the white region, whereby a reflected shock forms upon rupture of the secondary diaphragm (i.e. the case shown in figure 5), and u_{s1} is seen to reduce compared to the basic expansion tube. It was an explicitly stated assumption of earlier studies (Morgan 2001*a*) that the secondary driver gas must unsteadily expand into the test gas in order to utilise its higher sound speed to drive a stronger shock. Nevertheless, observing figure 9(*b*), it becomes evident that for X2 operating with an air test gas, even though the secondary driver is over-tailored over most of the sensible facility operating envelope, the requirement that the shock-processed secondary driver gas (region $sd2$) must undergo an unsteady expansion into the test gas to achieve a performance increase becomes very restrictive.

The dark grey lower right corner region in figure 9(*b*) indicates combinations of low secondary driver and high shock tube fill pressures which lead to non-standard solutions, and which represent neither practical nor useful configurations of the facility.

Ten points are shown in figure 9(*b*) (points *a–k*) which provide indicative fill pressures and shock speeds for operation through the high-performance region for this example configuration. Details of the points are provided in table 2. Three rows of points – (*c–e*), (*f–h*) and (*i–k*) – correspond to shock tube fill pressures of $p_1 = 10\,000$, 1000 and 100 Pa, respectively. The first and third points from each row (i.e. those points lying on the intersection lines) represent secondary driver operation which theoretically produces the same shock speed as operation without the device, i.e. no performance increase. Each middle point represents secondary driver operation
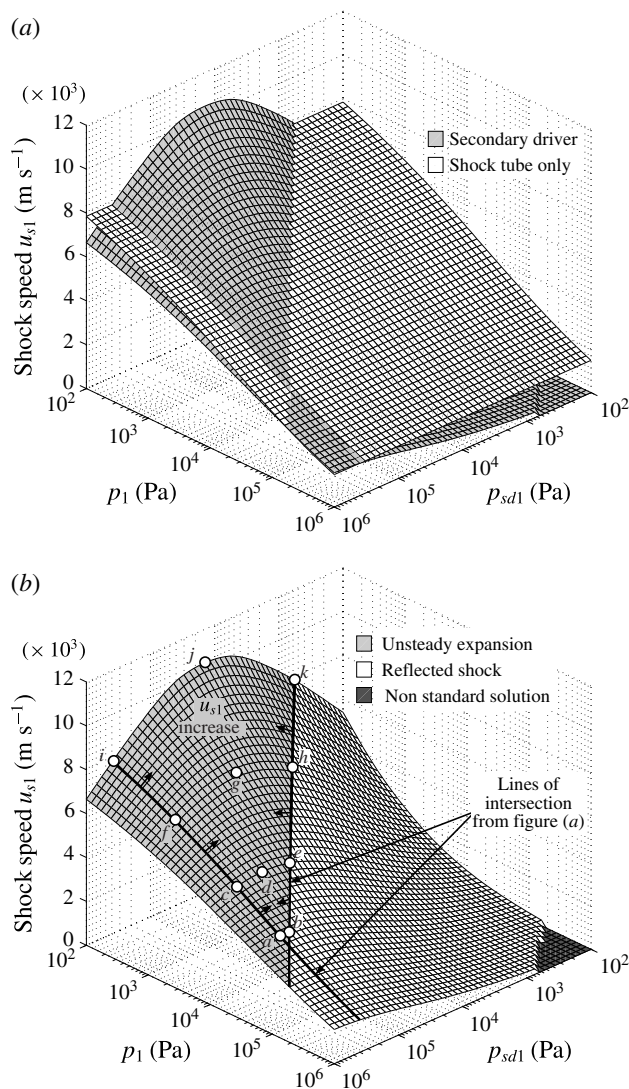
FIGURE 9. Computed shock tube speeds through air test gas for different combinations of helium secondary driver and shock tube fill pressures, for driver condition x2-lwp-2.0mm-100He-0 from Gildfind *et al.* (2015) (see table 1); (*a*) compares computed test gas shock speeds for operation with and without a secondary driver; (*b*) shows the region of the performance envelope where the secondary driver produces a performance increase, as well as regions where performance is reduced; shading in (*b*) indicates the predicted secondary diaphragm flow process (either an unsteady expansion, reflected shock wave, or non-standard solution); points marked *a–k* provide indicative facility configuration details, and are summarised in table 2.

which leads to the maximum shock speed for each given p_1. Referring to shock speeds in table 2, for $p_1 = 1000$ Pa the secondary driver can increase shock speed by a maximum of 14 %. For $p_1 = 100$ Pa, the increase is 33 %. Observing point *d*, and finally points *a* and *b*, it can be seen that no useful performance increase is achieved for high p_1 and low u_s.

Point (—)	p_{sd1} (Pa)	p_1 (Pa)	u_{s1} (m s^{-1})
a	382 102	50 000	3 523
b	283 167	50 000	3 523
c	389 907	10 000	4 833
d	158 500	10 000	4 991
e	57 925	10 000	4 833
f	390 394	1 000	6 525
g	43 650	1 000	7 450
h	5 700	1 000	6 525
i	390 547	100	7 850
j	14 450	100	10 470
k	571	100	7 850

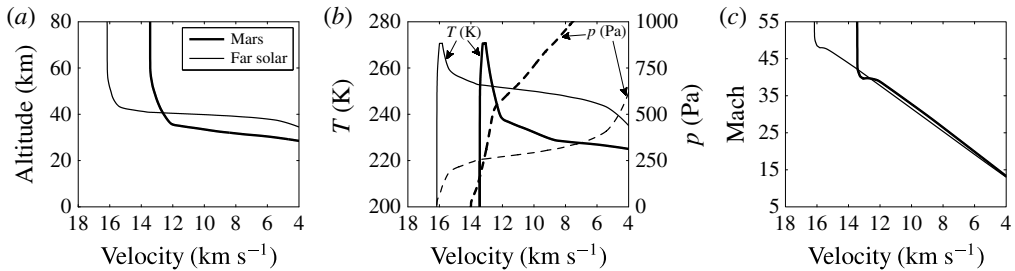TABLE 2. Selected datapoints from figure 9(*b*).

FIGURE 10. Representative Mars and Far Solar System return re-entry trajectories (NASA 2010). In each plot, thick curves represent Mars return trajectory properties; thin curves represent Far Solar System return: (*a*) return trajectories; (*b*) US standard atmosphere; (*c*) computed Mach number.

5. Representative flow conditions

The physical implications of the figure 9 results can be better understood by examining some representative flow conditions. Both high- and low-enthalpy conditions are now considered.

5.1. *High-enthalpy flight*

Expansion tubes provide an experimental tool to conduct studies of radiative heating around blunt bodies. Representative Mars and Far Solar System return re-entry trajectories from NASA (2010) are shown in figure 10. These are the hypervelocity, low density, flight conditions through air which a vehicle returning to Earth's atmosphere would undergo. These currently can only be produced by an expansion tube, and at the upper limits they may depend on the performance increase provided by the secondary driver.

For Mars return at 13 km s^{-1}, the altitude is 46.1 km, the Mach number is 39.7, with temperature 267 K and static pressure 130 Pa. To achieve this flow condition with an expansion tube, p_1 must be exceedingly low in order to attain such a high speed and simultaneously very low temperature; it is impractical to operate at such

low test gas pressures in expansion tubes, since viscous effects in the low-pressure acceleration tube corrupt the test flow (Mirels 1963a,b).

Ground testing at these conditions takes advantage of the commonly accepted Mach number independence principle. This states that, at high Mach numbers, aerodynamic characteristics such as flow field structure, pressure coefficients, lift, drag, and so forth, become asymptotically independent of Mach number (Kliche, Mundt & Hirschel 2011; Anderson 2006). While the validity of this principle has been questioned for high-Mach-number viscous flows (Kliche *et al.* 2011), this commonly accepted principle relaxes the requirement to simulate re-entry flows at true flight Mach numbers. It becomes necessary only to achieve sufficiently high Mach numbers for the independence principle to apply, which for blunt-body flow is met for Mach numbers greater than five (Anderson 2006, figure 4.2).

Considering the 13 km s^{-1} Mars return trajectory, and assuming equilibrium gas properties, if the flow is expanded to just Mach 10, its temperature will be significantly higher (Mach 10 at 13 km s^{-1} corresponds to an equilibrium free-stream temperature of 4621 K, with specific heat at constant pressure, $c_p = 1339$ J kg^{-1} K^{-1}; calculated using CEA). Noting that total temperature and total enthalpy are conserved across the vehicle bow shock, to conserve total temperature it can be necessary for the experiment to account for the increased static enthalpy of the expansion tube free-stream test flow in comparison to true flight. Equating true flight ('∞') and expansion tube ('e') total enthalpies:

$$c_p T_\infty + \frac{U_\infty^2}{2} = c_p T_e + \frac{U_e^2}{2}. \quad (5.1)$$

Neglecting the static enthalpy of the true flight free-stream flow ($c_p T_\infty \approx 0$), the target expansion tube test flow velocity, U_e, is calculated as follows:

$$U_e = \sqrt{U_\infty^2 - 2 c_p T_e}. \quad (5.2)$$

U_e is the flight equivalent velocity, and indicates that expansion tube simulation requires a marginally lower velocity than true flight. For 13 km s^{-1} flow at $T = 4621$ K, U_e is only 4 % less than U_∞, indicating that most of the enthalpy is associated with the flow kinetic energy:

$$U_e = \sqrt{13\,000^2 - 2 \times 1334 \times 4625} = 12\,516 \text{ m s}^{-1}. \quad (5.3)$$

Neglecting the difference between U_e and U_∞ for the purposes of this present study, and assuming absolute viscosity, μ, is conserved between true flight and experiment, Reynolds number is preserved for a blunt-body vehicle if the product ρL is also conserved, where ρ is the density behind the shock and L is the characteristic length (for a planetary entry vehicle this might be the nose radius).

$$Re = \frac{\rho U L}{\mu}. \quad (5.4)$$

For the true flight case, the equilibrium properties behind a normal shock are summarised in table 3. It can be seen that expansion tube simulation requires that the density of the flow behind the shock, ρ, be equal to 0.0258 kg m^{-3}. For the expansion tube test flow with temperature of 4621 K and $U_e = 13\,000$ m s^{-1}, this corresponds to a free-stream static pressure of $p_e = 2380$ Pa. Whereas the 130 Pa

Flow property	Pre-shock	Post-shock
Velocity, u (m s^{-1})	13 000	12 144
Temperature, T (K)	267	14 366
Static pressure, p (kPa)	0.130	268
Density, ρ (kg m^{-3})	0.00170	0.0258
c_p (J kg^{-1} K^{-1})	1004	15 708
γ	1.401	1.184

TABLE 3. Pre- and post-shock flow properties for Mars return re-entry trajectory at 13 km s^{-1}.

				True flight				Mach 10 free-stream equivalent	
		u	T	p	ρ	c_p	γ	T	p
		(m s^{-1})	(K)	(kPa)	(kg m^{-3})	(J kg^{-1} K^{-1})	(—)	(K)	(kPa)
11 km s^{-1}	Pre-shock	11 000	235	0.624	0.00925	1 003	1.401	3287	9.00
	Post-shock	10 204	13 213	1039	0.128	6 995	1.208		
12 km s^{-1}	Pre-shock	12 000	238	0.53	0.00776	1 003	1.401	3925	9.21
	Post-shock	11 140	14 561	1038	0.108	10 107	1.2		
13 km s^{-1}	Pre-shock	13 000	267	0.13	0.0017	1 004	1.401	4621	2.38
	Post-shock	12 144	14 366	268	0.0258	15 708	1.184		

TABLE 4. Mars return re-entry trajectory flow properties, calculated from figure 10.

				True flight				Mach 10 free-stream equivalent	
		u	T	p	ρ	c_p	γ	T	p
		(m s^{-1})	(K)	(kPa)	(kg m^{-3})	(J kg^{-1} K^{-1})	(—)	(K)	(kPa)
13 km s^{-1}	Pre-shock	13 000	252	0.26	0.00359	1 003	1.401	4620	5.03
	Post-shock	12 111	15 052	566	0.0525	14 109	1.193		
14 km s^{-1}	Pre-shock	14 000	254	0.24	0.00329	1 003	1.401	5370	5.37
	Post-shock	13 054	15 998	602	0.0487	16 233	1.199		
15 km s^{-1}	Pre-shock	15 000	257	0.208	0.00282	1 003	1.401	6185	5.32
	Post-shock	13 998	16 832	592	0.0422	17 449	1.207		
16 km s^{-1}	Pre-shock	16 000	270	0.065	0.00084	1 004	1.401	7070	1.82
	Post-shock	14 999	16 405	201	0.0134	19 187	1.206		

TABLE 5. Far Solar System return re-entry trajectory flow properties, calculated from figure 10.

free-stream static pressure at Mach 39.7 is impractical to achieve in an expansion tube, 2380 Pa at Mach 10 becomes more feasible.

The process detailed above was used to calculate Mach 10 equivalent flow conditions for both Mars and Far Solar System return trajectories; results are summarised in tables 4 and 5. These are fairly representative of the type of high-enthalpy flow conditions for which expansion tubes would typically be used.

Mach (—)	Altitude (m)	T (K)	V (m s^{-1})	h (MJ kg^{-1} K^{-1})	p (kPa)	p_0 (MPa)
10	29 108	226	3011	4.76	1.368	128
12	31 552	228	3633	6.52	0.950	457
14	33 649	233	4282	9.10	0.698	1469

TABLE 6. 95.8 kPa scramjet flow conditions. Free-stream properties have been calculated using the American Standard Atmosphere 1976 (COESA 1976); total pressure has been calculated using equilibrium gas properties with the NASA code CEA (Gordon & McBride 1994) in accordance with Chinitz *et al.* (1994).

5.2. *Low-enthalpy flight*

The scramjet engine is viewed as a potential source of launch vehicle propulsion between Mach 4 and 15 (Curran 2001). Most scramjet trajectory studies propose that the launch vehicle should target an approximately constant dynamic pressure trajectory during the scramjet burn cycle (Olds & Budianto 1998). The magnitude of this dynamic pressure determines the structural and heat loading to the engine, and several authors consider that the representative upper limit for this is around 2000 psf (95.8 kPa) (Billig 1993; Hicks 1993; Olds & Budianto 1998; Hunt & Martin 2000).

Table 6 shows scramjet access-to-space flight conditions at Mach 10, 12 and 14, for a 95.8 kPa dynamic pressure trajectory. It can be seen that, for Mach 10 flight, the full-scale equilibrium free-stream total pressure is 128 MPa, which is approaching the upper limit of RST facilities (Bakos & Erdos 1995). At Mach 14 the total pressure increases by an order of magnitude, to gigapascal levels.

Scramjet ground testing is typically undertaken using sub-scale engine models. Pressure–length scaling (p–L scaling, which is binary scaling at constant temperature) is applied to maintain similarity for Mach number, enthalpy, Reynolds number and binary reactions (Stalker & Pulsonetti 2004). p–L scaling requires increasing test flow static pressure in inverse proportion to any decrease in model length, so that sub-scale models require even higher static pressures compared to true flight. This means that the actual test flow total pressures required at high Mach numbers may be several times higher than those presented in table 6.

The expansion tube is currently the only ground testing facility able to produce the gigapascal total pressure flows associated with scramjet access to space beyond Mach 10. UQ's X2 facility has recently been used to generate scramjet test flows in the range Mach 10–14, up to a maximum total pressure of 10.4 GPa (Gildfind *et al.* 2014). X2 is a medium-sized free-piston-driven expansion tube; it has a total length of 23 m, and a driven tube bore diameter of 85 mm. Gildfind *et al.* (2014) was a proof-of-concept study undertaken to establish the feasibility of producing these flows in an expansion tube. Major outcomes included identification of the need for tuned operation of the free-piston driver (Gildfind *et al.* 2011) and the close coupling of wave processes at low-enthalpy flow conditions (Gildfind *et al.* 2014). These considerations were successfully addressed, and subsequent and ongoing work has been to scale these conditions to the larger 65 m X3 facility, which can provide the longer test times and larger test flow core diameters required for practical engine testing (Gildfind *et al.* 2013, 2014).

Although high-Mach-number scramjet flight takes place at relatively low enthalpies (4.5–12.5 MJ kg^{-1}; 3–5 km s^{-1}) compared to other expansion tube applications

(18–200 MJ kg^{-1}; 6–20 km s^{-1}), their massive total pressures make expansion tubes an important tool for ground testing of these engines. The flow conditions detailed in table 6 are predominantly representative of the low-enthalpy flow conditions for which expansion tubes will be used in the coming years.

6. Flow condition mapping

It is recalled that the primary performance challenge for developing an expansion tube flow condition is achieving the required u_{s1} for a given p_1. Ignoring viscous effects, if the required u_{s1} can be achieved, then the acceleration tube simply has to be set to an appropriately low p_5, to bound the test gas unsteady expansion.

This section presents the results of an equilibrium gas expansion tube analysis used to calculate the theoretically required test gas shock speeds and fill pressures to achieve each of the flow conditions detailed in tables 4–6. The entire analysis was repeated for each flow condition.

$\{p_1, u_{s,1}, p_5, u_{s,5}\}$ solution sets were calculated for $p_5 = 0.1$ Pa to >1000 Pa (depending on the specific flow condition). Each solution set theoretically corresponded to the same flow condition; the only difference would be the magnitude of the test flow static pressure, p_7.

At low enthalpies $u_{s,1}$ and $u_{s,5}$ remain constant, as does the ratio p_5/p_1, even when equilibrium gas properties are accounted for; however, all three parameters increasingly vary with p_7 once the target flight enthalpy becomes high, since the test and accelerator gas temperatures both become significant. The procedure to calculate the required shock speeds is summarised as follows:

(a) Noting that the post-shock accelerator gas flow velocity, u_6, is equal to the final test gas velocity, u_7, an iterative routine was established using CEA to calculate u_{s5} to achieve the required u_6.

(b) Assuming that the unsteady expansion between regions 2 and 7 is isentropic, CEA was used to calculate a case-consistent set of pressures and temperatures through the expansion. The first pressure value was the post-shock pressure calculated in Step (a); the first temperature value was the test gas temperature from either table 4, 5, or 6. The pressure was then increased in finely spaced increments up to an order of magnitude of 100 MPa, and CEA was used to calculate the corresponding temperatures, while maintaining the initial entropy.

(c) Working backwards from u_7, the change in flow velocity through the unsteady expansion, from u_7 to zero velocity (i.e. to a velocity less than u_2), was calculated with equation (6.1) (from McIntyre *et al.* 2001), using the case-consistent set of gas properties from Step (b). Equation (6.1) relates the differential change in gas velocity through the unsteady expansion, du, to the change in speed of sound, da, as follows:

$$\mathrm{d}u = -\frac{2}{\gamma_1 - 1}\,\mathrm{d}a. \qquad (6.1)$$

(d) As in §4, a look-up-table was populated with region 2 flow properties for a matrix comprised of test gas shock speeds varying between $u_{s,1} = 400$ and $11\,000$ m s^{-1}, with test gas fill pressures varying between $p_1 = 10^2$ and 10^6 Pa. Noting that the test gas always undergoes an unsteady expansion into the acceleration tube, $u_{s,1}$ was calculated for each $\{u_{s,5}, p_5, p_1\}$ combination. This entailed an iterative solution process which identified the unique combinations of p_1 and $u_{s,1}$ for which: (i) p_2, u_2 values intersected the p, u curves derived in Step (c); and (ii) had the same entropy as Step (b).
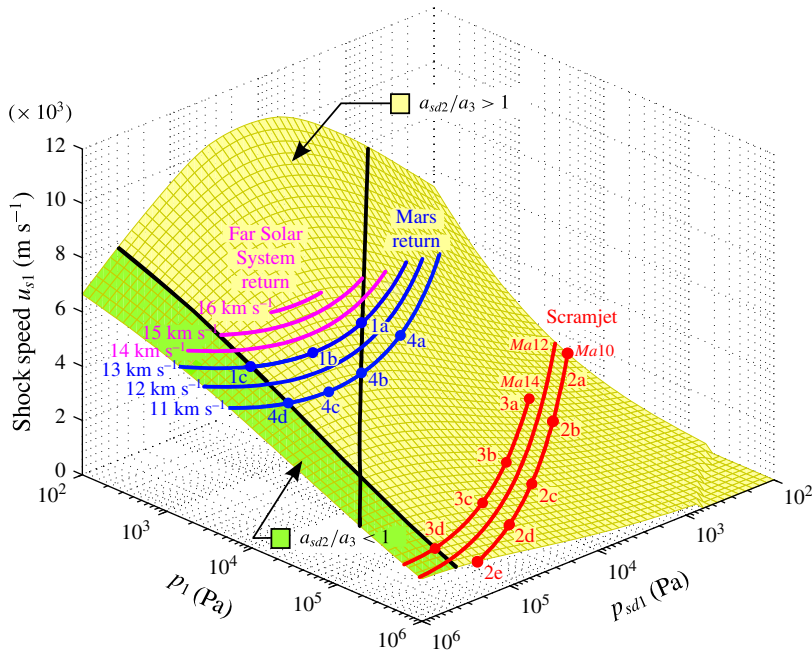
FIGURE 11. (Colour online) Flow conditions mapped onto performance envelope. Datapoints represent flow conditions that have been validated by experiment and/or CFD analysis; refer to table 7 for details of Case 1; table 9 for Case 2; table 10 for Case 3; table 8 for Case 4.

An accurate and consistent equilibrium analysis requires calculation of the entire solution set $\{p_1, u_{s,1}, p_5, u_{s,5}\}$ in order to determine the two variables of interest for this study, $\{p_1, u_{s,1}\}$. Once these are known, they can be compared against the X2 driver performance envelope previously shown in figure 9. Figure 11 shows each of the flow conditions from tables 4–6, mapped onto figure 9. Three key observations can be made:

(*a*) When a secondary driver is used, each target test condition can be achieved across a range of static pressures; there is a theoretical capacity to control the test flow static pressure even though the primary driver configuration is fixed.

(*b*) The majority of the low-enthalpy scramjet conditions are only achieved in a region of the facility operating envelope where the secondary driver reduces net performance, even though the secondary driver itself is over-tailored.

(*c*) As the flight enthalpy increases, the range of p_1 is reduced; for example, it can be seen that the 16 km s^{-1} Far Solar System return condition can be achieved only across a very narrow range of p_1. The reason for this is that the acceleration tube fill pressure was constrained to be $p_5 \geqslant 0.1$ Pa; this constraint was applied since viscous effects become overwhelming at fill pressures lower than this.

The results of figure 11 are now considered separately by examining in detail two of each of the high- and low-enthalpy conditions.

Case	p_{sd1} (kPa)	$u_{s,sd}$ (km s^{-1})	p_1 (kPa)	$u_{s,1}$ (km s^{-1})	p_2 (kPa)	p_5 (Pa)	$u_{s,5}$ (km s^{-1})	p_7 (kPa)	Shot I.D.
1a	22.4	6.91	3.83	5.59	1665	0.58	13.7	1.20	x2s2768
1b	112	5.30	5.43	5.61	2373	0.87	13.7	1.82	x2s2774
1c	398	4.04	3.74	5.59	1627	0.56	13.7	1.17	x2s2773
1d	—	—	3.74	5.59	1627	0.56	13.7	1.17	x2s2771

TABLE 7. Calculated facility operating parameters for Mars return 13 km s^{-1} Mach 10 equivalent flight.

7. Results and analysis

7.1. *High-enthalpy examples:* 13 *and* 11 km s^{-1} *Mars return*

Table 7 shows the calculated facility operating parameters for the 13 km s^{-1} Mars return case (Case 1 in figure 11). The test flow static pressure, p_7, is observed to vary with p_{sd1}, and achieves a peak of $p_7 = 1.82$ kPa for $p_{sd1} = 112$ kPa. Table 7 also shows p_7 for operation without a secondary driver; $p_7 = 1.17$ kPa for Case 1d. For this flow condition case, the secondary driver can theoretically provide an increase in test flow static pressure of up to 56 %.

For comparison, the Mach 10 true flight equivalent static pressure is 2.38 kPa (from figure 10), and is therefore marginally higher than what X2 can achieve with this specific free-piston driver condition. Nevertheless, these results confirm that the secondary driver can significantly outperform the basic expansion tube.

Figure 12(*a*) shows experimental confirmation of these results in X2. Measuring the speed of the primary shock as it traverses the length of the facility is an effective means to validate several of the key flow processes occurring during an experiment. It can be seen that there is generally good agreement with computed shock speeds through both the secondary driver and shock tube, although all except Case 1a have the experimental $u_{s,1}$ slightly less than the computed value.

It is noted that there is some scatter and uncertainty in the acceleration tube shock speeds; this was due to two reasons: firstly, the pressure sensors in this tube were insufficiently sensitive to precisely identify shock arrival at the transducer for these very low pressure conditions; secondly, low fill pressures could not be reliably achieved, or held, at the time of the experiments. Neither of these issues was of concern, since the important measurements were in the secondary driver and shock tube. However, these issues could be readily addressed in any future study requiring use of the final expanded test flow. Uncertainties in the secondary driver and shock tube are much lower, and in most cases the error bars, which are included in the plot, are too small to identify.

Figure 12(*b*) shows a tube wall static pressure measurement towards the end of the shock tube, p_2, for Cases 1a–1d. Comparing these traces to the computed value of p_2 in table 7, it can be seen that all four experimental traces are 10–20 % lower in magnitude. This discrepancy probably reflects the slightly lower experimental shock speeds which were measured in the shock tube. However, the important observation is that a significantly larger static pressure is observed for Case 1b compared to the other conditions, as predicted by table 7, confirming that the secondary driver can be used as a test gas static pressure control.

The same analysis was repeated for the 11 km s^{-1} Mars return condition (Case 4 in figure 11), with results shown in table 8 and figure 13. This example illustrates
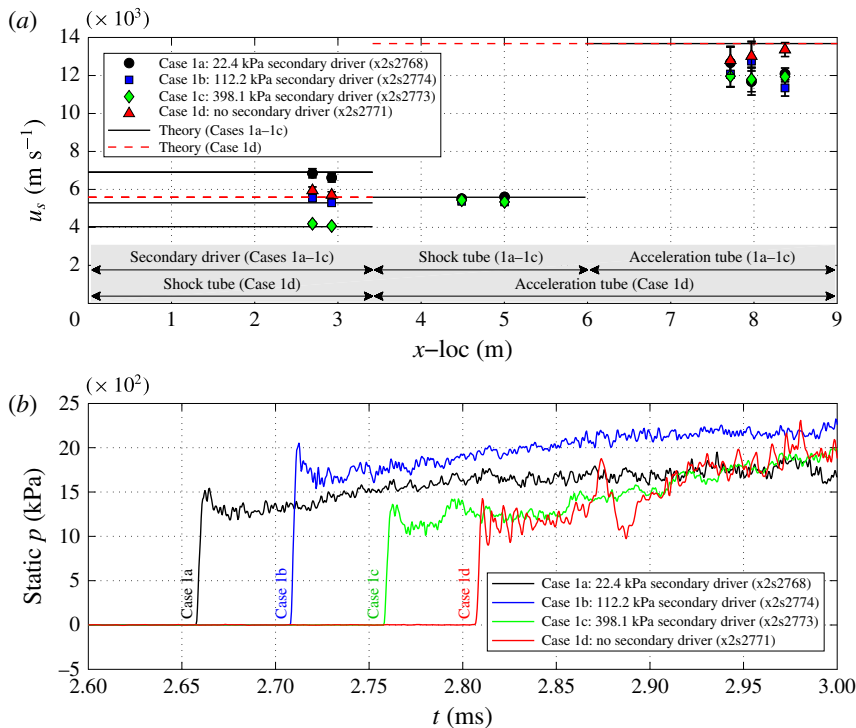
FIGURE 12. (Colour online) Experimental results for 13 km s^{-1} Mars return flight equivalent conditions; (*a*) shock speeds along the entire driven tube; (*b*) shock tube static pressures; static pressure traces are time-referenced to Case 1a, with offsets of 50 μs, 100 μs and 150 μs, for Cases 1b, 1c and 1d, respectively.

Case	p_{sd1} (kPa)	$u_{s,sd}$ (km s^{-1})	p_1 (kPa)	$u_{s,1}$ (km s^{-1})	p_2 (kPa)	p_5 (Pa)	$u_{s,5}$ (km s^{-1})	p_7 (kPa)	Shot I.D.
4a	10.0	7.67	4.71	4.79	1458	1.38	11.6	2.07	x2s2745
4b	55.2	6.01	10.0	4.82	3182	3.23	11.7	4.84	x2s2749
4c	159	4.95	11.9	4.83	3798	3.91	11.7	5.87	x2s2781
4d	398	4.04	10.1	4.82	3213	3.26	11.7	4.89	x2s2779
4e	—	—	10.1	4.82	3213	3.26	11.7	4.89	x2s2777

TABLE 8. Calculated facility operation parameters for Mars return 11 km s^{-1} Mach 10 equivalent flight.

how the secondary driver can be used to reduce performance. Referring to table 8, Case 1a theoretically has $p_7 = 2.1$ kPa, compared to $p_7 = 5$–6 kPa for Cases 1b–1e. This is reflected by a much lower static pressure in the shock tube (figure 13*b*); the relative difference is not as large as predicted by table 8, and is primarily due to the Case 4b experimental shock speeds being higher than the other conditions.

In summary, the 11 and 13 km s^{-1} Mars return results validate the driver characterisation detailed in Gildfind *et al.* (2015), and show that the analytical

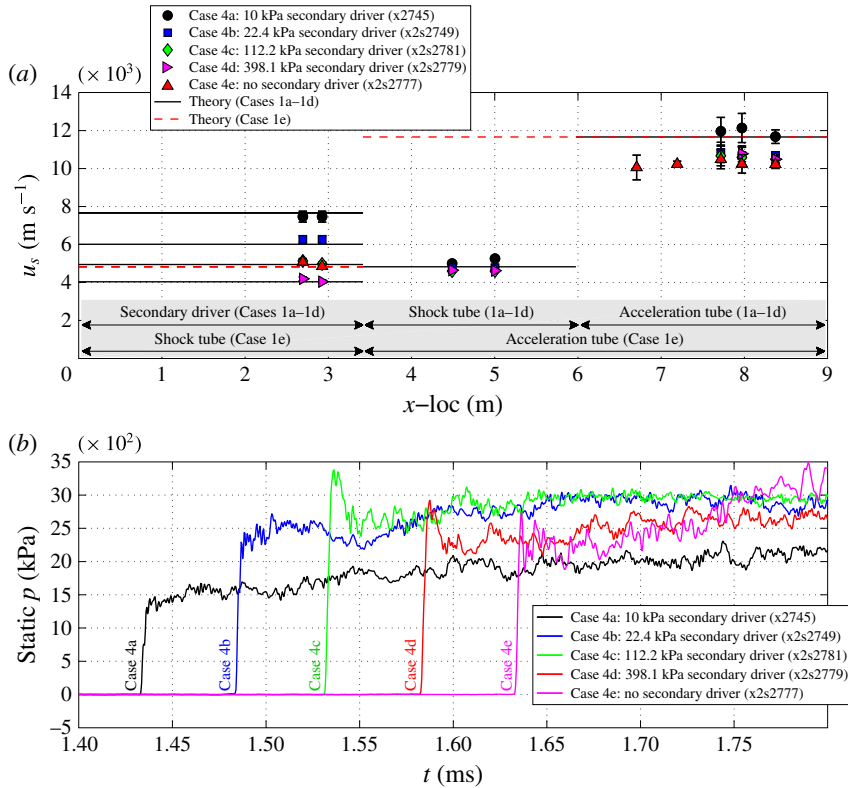FIGURE 13. (Colour online) Experimental results for 11 km s^{-1} Mars return flight equivalent conditions; (*a*) shock speeds along the entire driven tube; (*b*) shock tube static pressures; static pressure traces are time-referenced to Case 4a, with offsets of 50 µs, 100 µs, 150 µs and 200 µs for Cases 4b, 4c, 4d and 4e, respectively.

techniques presented in this paper correctly predict the trends for facility performance, both with and without a secondary driver, and show that test gas static pressure can be controlled using the secondary driver.

7.2. *Low-enthalpy examples: Mach* 10 *and Mach* 14 *scramjet flight*

Tables 9 and 10 show calculated facility parameters for the Mach 10 (Case 2) and Mach 14 (Case 3) scramjet flow conditions from figure 11. However, recent experience with these conditions (Gildfind 2012; Gildfind *et al.* 2014) has shown that these calculations become invalid for facility configurations when there is a strong reflected shock through the secondary driver gas. Referring to figure 14 (originally from Gildfind *et al.* 2014), when the secondary diaphragm ruptures, the shock-processed slug of helium (region *sd*2) has a short length but high sound speed, and is rapidly processed by the reflected shock wave (*c* in the figure). This wave then reflects off the *sd*2/*sd*3 interface, and returns as a strong compression wave (*d* and *e* in figure 14). The time scales for this phenomenon are very short compared to other flow processes; for most practical conditions, the secondary driver would need to be an order of magnitude longer than the shock tube to sufficiently delay
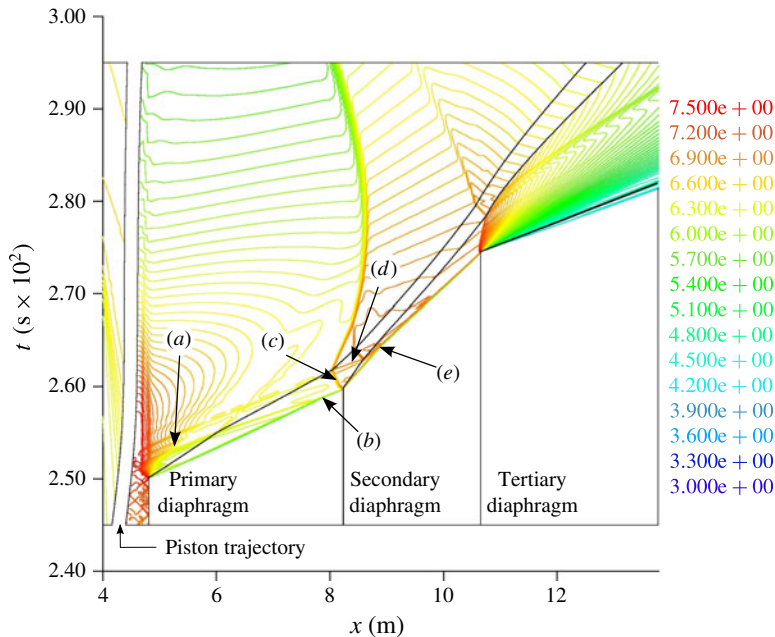
FIGURE 14. (Colour online) L1d-computed x–t diagram for Mach 10 scramjet flow condition in X2. Contours show log of static pressure (in units log (Pa)). (Points on x–t diagram: (*a*) Primary diaphragm is downstream of driver area change; compression wave is transmitted downstream from this area change. (*b*) Arrival of compression wave at primary shock increases shock speed. (*c*) Reflected shock arises at secondary diaphragm due to primary shock arrival at dense test gas. (*d*) Reflected shock hits contact surface and a second compression wave is sent downstream. (*e*) Second compression wave arrives at primary shock and causes a second primary shock speed increase.) Adapted from Gildfind *et al.* (2014, figure 9).

arrival of this wave. These wave processes have been described in Gildfind *et al.* (2014); however, the broader implications of those results were not examined at the time.

In practice, at low-enthalpy conditions with a dense test gas, the secondary driver behaviour is no longer adequately described by traditional theoretical models. The helium has negligible effect on the magnitude of test flow properties, and acts as a passive slug between the primary driver and test gases. This effect is shown in figure 15(*a*,*b*) for the Case 2 scramjet Mach 10 condition. In both plots, the 1-D computational fluid dynamics (CFD) code L1d (Jacobs 1994) has been used to calculate shock speeds along the length of X2, where $x = 0$ corresponds to the primary diaphragm location. These L1d models use a constant volume driver (with initial temperature and pressure as defined in table 1), instead of a free-piston driver, in order to provide a more direct comparison to the analytical calculations summarised in figure 11. The driver length in the L1d model was made sufficiently long to avoid interference of the reflected driver $u + a$ wave during the useful test time.

Referring to figure 15(*a*), the Case 2a–2e curves show shock speeds when secondary drivers of differing fill pressures are introduced between the primary diaphragm ($x = 0$) and $x = 3.4$ m; the case 2f curve shows the shock speed for a Mach 10 scramjet
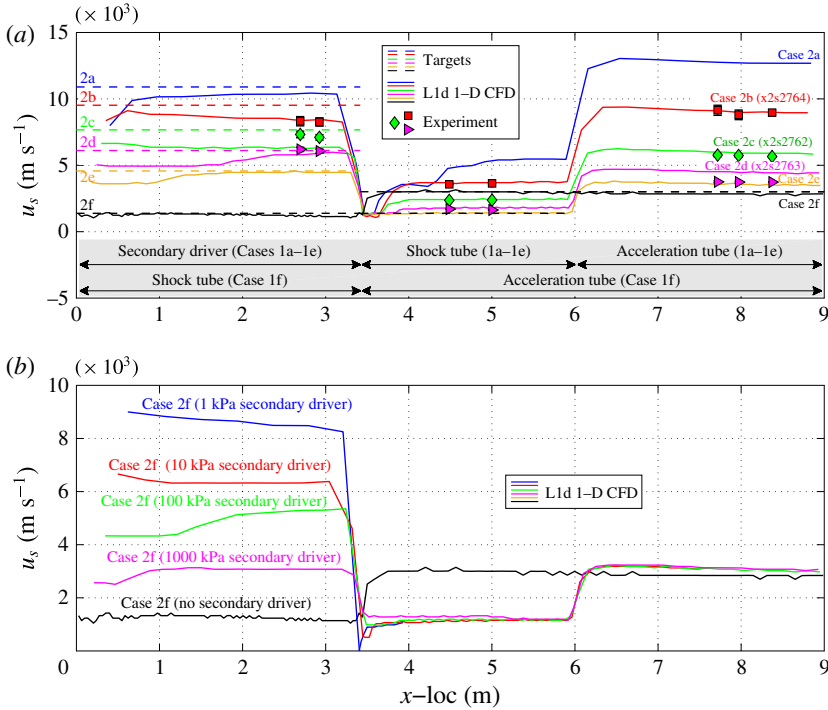
FIGURE 15. (Colour online) Shock speeds for X2 Mach 10 scramjet flow conditions detailed in table 9; (*a*) shows shock speeds for Cases 2a–2f; solid lines are L1d CFD calculations; dashed lines are calculated using the equilibrium analysis in § 6; datapoints are experimental results; (*b*) shows L1d shock speeds for Case 2f operated with and without a secondary driver, for a wide range of secondary driver fill pressures.

Case	p_{sd1} (kPa)	$u_{s,sd}$ (km s^{-1})	p_1 (kPa)	$u_{s,1}$ (km s^{-1})	p_5 (Pa)	$u_{s,5}$ (km s^{-1})	p_7 (kPa)	Shot I.D.
2a	0.100	10.9	3.76	1.38	1.61	3.31	0.188	—
2b	1.00	9.52	28.2	1.38	12.0	3.33	1.41	x2s2764
2c	10.0	7.67	165	1.38	69.5	3.35	8.26	x2s2762
2d	50.1	6.11	472	1.38	198	3.36	23.6	x2s2763
2e	231	4.57	1000	1.38	420	3.37	50.1	—
2f	—	—	1551	1.38	651	3.31	75.0	—

TABLE 9. Calculated facility configurations for Mach 10 scramjet flight.

condition without a secondary driver. Dashed lines show the corresponding 'target' shock speeds at each condition; these are the shock speeds predicted by analytical techniques (see table 9), which should theoretically achieve the flow conditions shown in figure 11. It is clear in figure 15(*a*) that the L1d-computed shock speeds match the target speeds reasonably well through the secondary driver; however, L1d predicts higher shock speeds through the downstream shock and acceleration tubes.

Case	p_{sd1} (kPa)	$u_{s,sd}$ (km s^{-1})	p_1 (kPa)	$u_{s,1}$ (km s^{-1})	p_5 (Pa)	$u_{s,5}$ (km s^{-1})	p_7 (kPa)	Shot I.D.
3a	1.00	9.54	14.3	1.81	1.09	4.65	0.255	x2s2767
3b	10.0	7.67	83.8	1.81	6.35	4.67	1.49	x2s2766
3c	50.1	6.11	233	1.81	17.6	4.68	4.13	x2s2782
3d	398	4.04	548	1.81	41.3	4.69	9.75	x2s2758
3e	—	—	548	1.81	41.3	4.69	9.75	x2s2759

TABLE 10. Calculated facility configurations for Mach 14 scramjet flight.

L1d, which has been shown to reliably predict shock speeds in recent scramjet flow condition studies using UQ's X2 and X3 facilities (Gildfind 2012; Gildfind *et al.* 2013, 2014), takes into account the full set of longitudinal wave processes. As with the Gildfind *et al.* (2014) study, the reinforcing compression wave from the driver, which is captured by L1d, causes an increase in the shock speed above the target level. Referring to the red '*Ma*10' curve in figure 11, it can be seen that as the secondary driver fill pressure is reduced, the secondary driver is predicted by analytical techniques to become increasingly ineffective at driving a shock into the air test gas. This explains why the downstream fill pressures in table 9, p_1 and p_5, become correspondingly lower in order to achieve the same shock speeds. However, since the reinforcing compression wave (d and e in figure 14) essentially restores the full strength of the driver, then higher shock speeds are predicted at these lower fill pressures in figure 15.

Figure 15(*b*) demonstrates the ineffectiveness of the secondary driver at lower enthalpies from a different perspective. This figure shows L1d-computed shock speeds for flow condition 'Case 2f', which is designed for X2 without a secondary driver. The black curve in figure 15(*b*) is shown to match the 'target' shock speeds very closely (note, for this L1d simulation the shock tube runs from $x = 0$ to $x = 3.4$ m). The other curves show shock speeds for the same condition, except in each case a helium secondary driver is introduced between $x = 0$ and $x = 3.4$ m. Each of these curves represents a different secondary driver fill pressure, across a range spanning 1–1000 kPa. While computed shock speeds evidently vary through the secondary driver, all curves are seen to collapse to the same speeds further downstream in the shock tube. This result shows that the final magnitude of the test flow properties is unaffected by the inclusion of a helium secondary driver once driver secondary wave processes are accounted for. Thus the theoretical predictions of figure 11 are shown to be invalid. At low enthalpies, where a reflected shock processes the secondary driver gas, the theoretical test gas shock speed is not achieved due to the driver wave coupling.

Referring to figure 15(*a*), it is noted that shock speeds for Cases 2b–2d have been validated by experiment with X2, and good agreement is observed. Error bars are plotted but are not obvious since experimental uncertainties for these shock speeds are low. The remaining shock speeds in figure 15(*a,b*) were not experimentally validated due to the impractical shock tube fill pressures required for these conditions (100 Pa for Case 2a; 1551 kPa for all of the Case 2f conditions). The 1551 kPa fill pressure exceeds the current manifold and instrumentation pressure rating for X2, and is only required to be this high in the example to match the high performance of this particular free-piston driver condition.
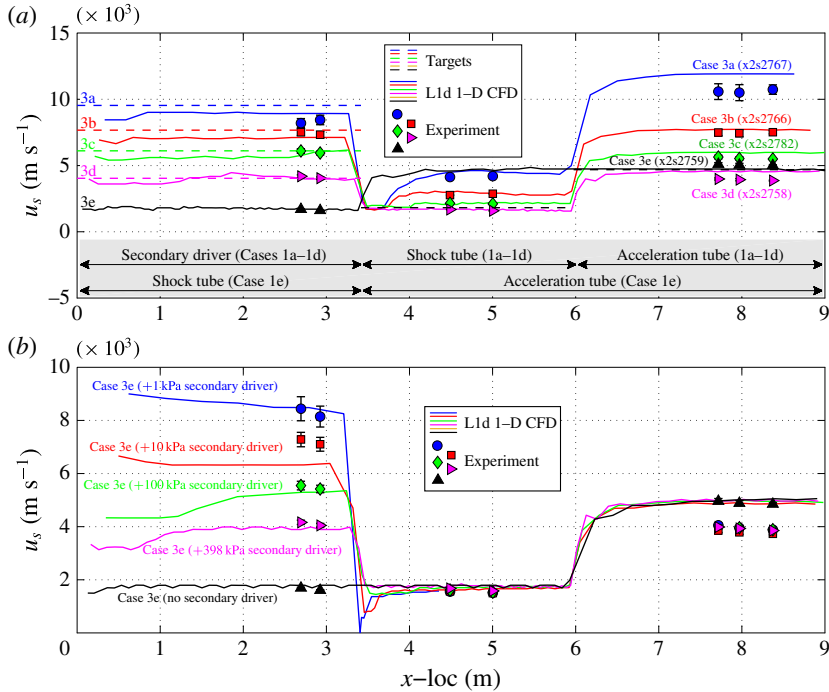
FIGURE 16. (Colour online) Shock speeds for X2 Mach 14 scramjet flow conditions detailed in table 10; (*a*) shows shock speeds for Cases 3a–3e; solid lines are L1d CFD calculations; dashed lines are calculated using the equilibrium analysis in §6; datapoints are experimental results; (*b*) shows L1d shock speeds for Case 3e operated with and without a secondary driver, for a wide range of secondary driver fill pressures; datapoints are experimental results.

More comprehensive validation was undertaken for the Mach 14 flow condition. Figures 16(*a,b*) are Mach 14 equivalents of the figure 15(*a,b*) Mach 10 plots. Full validation at Mach 14 was possible since the maximum shock tube fill pressure was lower (548 kPa). Identical trends are observed in figure 16, thereby supporting earlier conclusions about the secondary driver operation at low-enthalpy conditions. The computed shock speeds match experiment closely through the secondary driver and shock tube. Case 3e (no secondary driver) also indicates good agreement between L1d and experiment; however, all of the secondary driver conditions have slower experimental shock speeds through the acceleration tube than those predicted by L1d. The cause of this discrepancy was not established, since the secondary driver and shock tube measurements were the most relevant results for this secondary driver study, and examination of acceleration tube flow processes would have required computationally intensive axisymmetric CFD of the facility, across several conditions. However, a consistent difference with the secondary driver conditions was the relatively short acceleration tube, arising due to the addition of a third diaphragm. With a shorter acceleration tube the test flow is more influenced by shock establishment and interface mixing, and the test gas is not fully utilised. This issue would need to be re-examined before X2 was used for these specific operating conditions, and normally extension tubes would be added to lengthen the acceleration tube for such experiments.
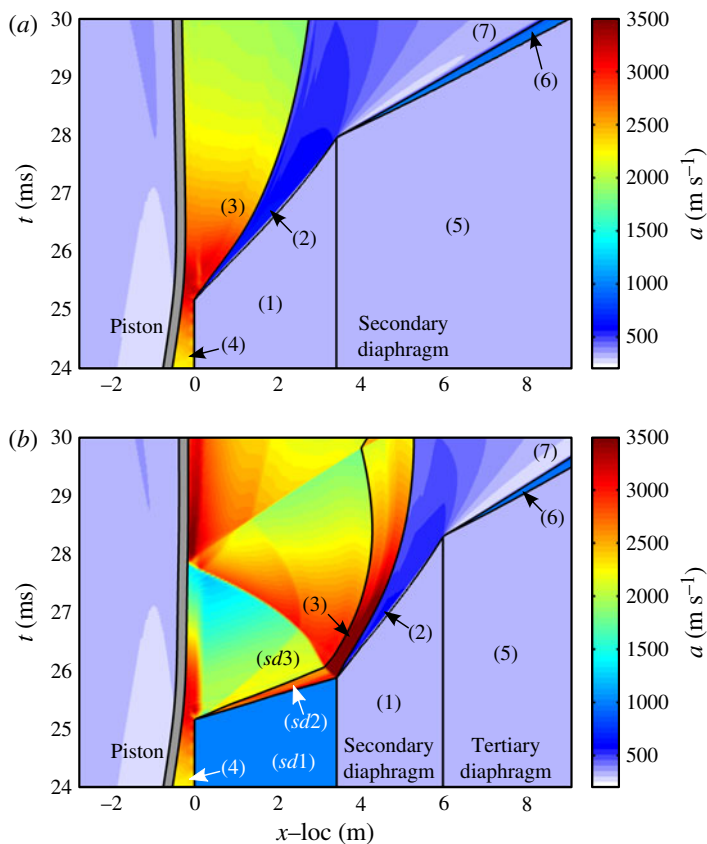
FIGURE 17. (Colour online) Computed sound speed for Mach 10 scramjet condition (*a*) without and (*b*) with 150 kPa helium secondary driver.

7.3. *Secondary driver as acoustic buffer, and test time implications*

As discussed in § 2.3, Morgan & Stalker (1991) proposed the use of a secondary driver to act as an 'acoustic buffer' for these types of scramjet conditions, because it had earlier been shown that over-tailored operation could prevent the transmission of driver disturbances from the expanded primary driver gas to the test gas (Paull & Stalker 1992). Figure 17 demonstrates this 'acoustic buffer' using L1d simulations of X2, incorporating full piston dynamics, for the 'case 2f' Mach 10 condition in figure 15 and table 9. Figure 17(*a*) shows sound speed mapped over an *x*–*t* diagram for the basic expansion tube; figure 17(*a*) shows the same result with a helium secondary driver initially at 150 kPa. It can be seen that, without a secondary driver, the ratio $a_2/a_3 \ll 1$, and driver noise would be expected to transmit to the test gas (Paull & Stalker 1992); figure 17(*b*), however, shows that the inclusion of a secondary driver strongly over-tailors the interface to the primary driver gas (i.e. $a_{sd2}/a_{sd3} \gg 1$), thereby meeting the acoustic buffer requirement.

While this arrangement would theoretically shield the downstream gas from primary driver disturbances, the air (region 2) is still under-tailored with respect to region 3; disturbances arising in the secondary driver gas due to Mylar diaphragm rupture, or the flow's passage down the tube, could theoretically be transmitted to the test gas this way. Since the test gas itself lacks the intrinsic mechanism to prevent noise ingress, it

might be expected that these conditions should be somewhat noisier than conditions where the test gas itself provides the acoustic buffer. Furthermore, for scramjet flow conditions, the secondary driver gas will be processed by a reflected shock, and the effect, if any, of this shock on transmission of acoustic disturbances has not been studied in detail.

Recalling figure 16(*b*), the Mach 14 scramjet flow condition, Case 3e, was experimentally tested with and without a secondary driver, and at a range of different secondary driver fill pressures. For these experiments a flow impact pressure measurement was made at the tube exit using 15° half-angle cone probes. These probes are described in Gildfind *et al.* (2014), and were developed for earlier scramjet flow condition testing. The probe has a conical face in order to reduce heating, pressure loading and impact damage to the transducer sensing face, and to provide a generally less severe measurement than a blunt-body Pitot probe. Two probes were placed at radial offsets of ± 9 mm around the tube centreline, in accordance with the configuration shown in figure 18(*a*); cone pressure measurements are shown in figure 18(*b–f*) for the cases shown in figure 16(*b*).

Figure 18(*b*) shows the cone pressure traces for Case 3e without a secondary driver. A 100 μs period of approximately steady cone pressure (≈ 100 kPa) is identified on the two traces. Through this region high-frequency noise can be observed, causing a fluctuation of approximately $\pm 10\,\%$ about the mean. After this period of identified test time, the cone impact pressure rises due to the test gas being underexpanded, higher temperature, lower Mach number, and therefore departing too far from the target flow condition.

The same condition is then shown with a range of secondary driver fill pressures in figure 16(*c–f*). Unsurprisingly, all of these cone pressure traces have a similar magnitude, which is lower than figure 16(*b*), and which is consistent with the lower experimental shock speeds shown in figure 16(*b*). Two differences are apparent; firstly, each cone pressure is increasing during the passage of the test gas, which arrives after the accelerator gas (the accelerator gas is the initial region of low impact pressure). For the purposes of comparison, the region of test time is identified as the region where cone pressures are 50–100 kPa; however, a test gas with this pressure gradient would not be useful for practical experiments. The test time according to this definition is approximately half the duration of the case without a secondary driver.

The second observation is that figures 16(*c–e*) do not exhibit the high-frequency noise of figure 16(*b*). This supports the argument that the secondary driver has suppressed disturbance transmission to the test gas. Observing 16(*f*), this is actually Case 3d; observing figure 11, the driver sound speed ratio is matched at this condition ($a_{sd2} = a_3$), therefore this condition would be expected to be noisier, and this is observed.

The results from figure 16 suggest that further analysis is required to validate the acoustic buffer function of the secondary driver. While the secondary driver appears to reduce high-frequency noise in the cone pressure traces, it can be seen in figure 16 that useful test time is significantly reduced, and the impact pressure measurements do not exhibit a suitable period of test gas with steady flow properties. Studying and optimising the acoustics and wave processes of this mode of operation is beyond the scope of the current paper, and is part of an ongoing separate investigation.

The short test times of 50–100 μs are not sufficient for scramjet engine tests, which usually require much longer duration test flows than high-enthalpy planetary entry
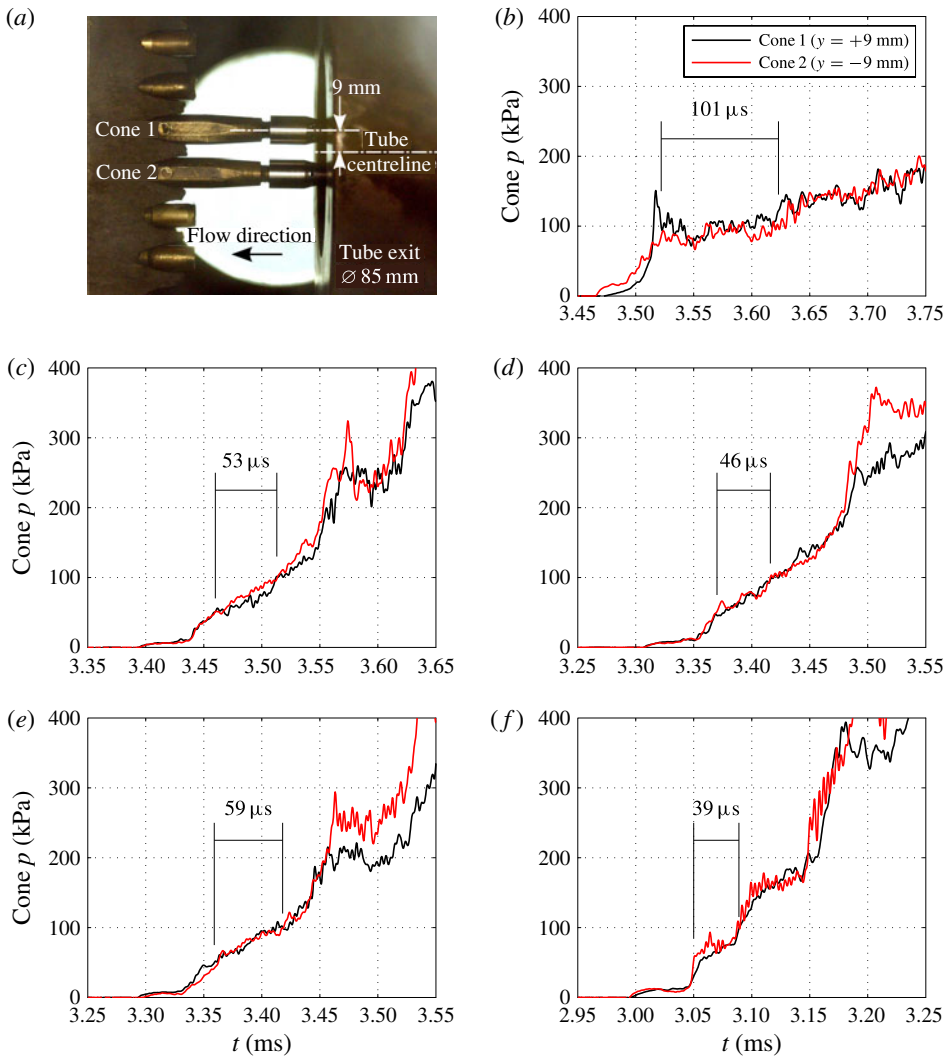
FIGURE 18. (Colour online) Cone pressures for X2 Mach 14 scramjet flow condition, Case 3e from table 10, operated with and without a secondary driver, for a wide range of secondary driver fill pressures: (*a*) cone probe configuration; (*b*) no secondary driver (shot x2s2784); (*c*) 1 kPa secondary driver (shot x2s2787); (*d*) 10 kPa secondary driver (shot x2s2788); (*e*) 100 kPa secondary driver (shot x2s2789); (*f*) 398 kPa secondary driver (shot x2s2757).

studies. Anderson, Kumar & Erdos (1990) suggests minimum test time requirements to achieve flow establishment inside a scramjet engine as follows:

$$tu/L \geqslant 2 \quad \text{for attached turbulent flow,} \tag{7.1}$$

$$tu/L \geqslant 3 \quad \text{for attached laminar flow,} \tag{7.2}$$

where t is the test time, u is the flow velocity and L is the overall model length. For a reasonably large 1 m long model at Mach 10 (3011 km s^{-1} from table 6), the test
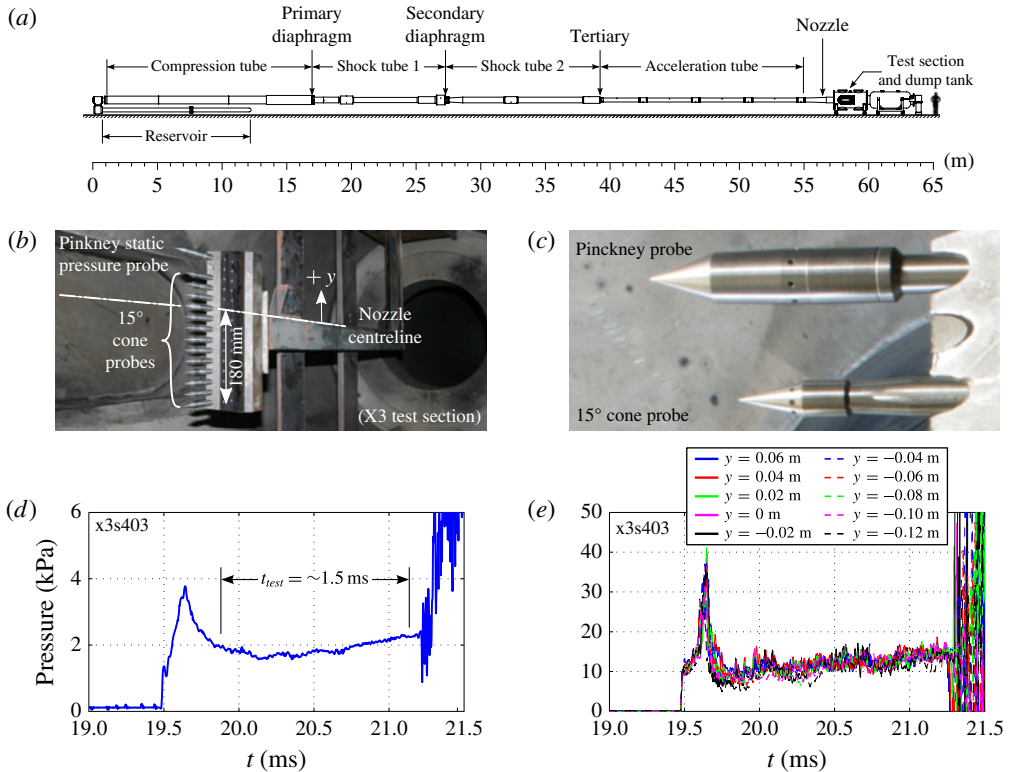
FIGURE 19. (Colour online) Details of X3 Mach 10 scramjet test flow experiment:
(*a*) X3 expansion tube facility schematic; (*b*) X3 Pitot rake arrangement; (*c*) probe detail;
(*d*) Pinckney probe pressure measurement; (*e*) cone probe pressure measurements.

time would therefore need to exceed $3 \times 1.0/3011 = 1$ ms, which is at least an order
of magnitude higher than the test times identified in figure 18. However, this does not
preclude expansion tubes from scramjet testing.

The high total pressure capability of expansion tubes allows testing of smaller
models through binary (ρ–L) scaling, and test time can also be increased through the
use of a contoured nozzle (Stewart, Jacobs & Morgan 2001). McGilvray *et al.* (2010)
used X2 in the basic expansion tube mode (no secondary driver) with a contoured
nozzle, to test a 2/5 scale, 0.5 m long 2-D scramjet. These results compared well
with tests of the full-scale engine in UQ's T4 RST facility, at equivalent ρ–L product.

For testing of larger engines, the problem of test time is directly addressed by using
a large facility. Scramjet engine testing in X2 (McGilvray *et al.* 2010) and X2 flow
condition development (Gildfind *et al.* 2014) were both conducted primarily as proof-
of-concept studies in preparation for scaling up to UQ's much larger free-piston-driven
X3 facility. At 65 m length, with a 183 mm acceleration tube bore, X3 has equivalent
total pressure capability to X2, but can test much larger models, and for significantly
longer test times.

Figure 19(*a*) shows a scaled drawing of X3, which has recently been used to
generate Mach 10 scramjet test flows in support of scramjet engine testing (Gildfind
et al. 2013). As part of the flow condition development process, nozzle exit flow
measurements were made with the Pitot rake shown in figure 19(*b*). This rake was

instrumented primarily with the cone probes also shown in figure 18, as well as a quasi-static-pressure 'Pinckney' probe (Pinckney 1975). Referring to figure 19(*d,e*), the useful test time is approximately 1.25 ms, with a core flow diameter of 200 mm (using X3's Mach 10 440 mm inner exit diameter nozzle). Noting that this condition used a secondary driver, cone impact pressures are much steadier than those shown in figure 18, although there remains a pressure gradient during the test time.

Figure 19 illustrates the potential for large expansion tubes to achieve an equivalent test time and model size capability to that of large RST facilities, but at much higher total pressures.

8. Key observations

Several observations have been made with respect to expansion tube operation with a secondary driver, which are summarised as follows:

(*a*) As previous analyses have shown (Henshall 1956; Stalker & Plumb 1968; Morgan & Stalker 1991; Morgan 2001*a*), an over-tailored secondary driver can drive a stronger shock than the primary driver by itself. The region of performance increase is bounded by two requirements: firstly, the secondary driver must be over-tailored, i.e. ($a_{sd2} > a_3$); secondly, the secondary driver gas must undergo an unsteady expansion upon impacting the test gas.

(*b*) Within the region of performance gain, the secondary driver can be used as a static pressure control. In a basic expansion tube, there is only one combination of test flow static pressure, temperature and velocity, which can be achieved with a fixed primary driver configuration. This study has shown that introducing a secondary driver allows test flow static pressure to be varied widely for otherwise identical flow conditions (in terms of velocity, temperature and, therefore, Mach number). Analytical calculations corrected for chemical equilibrium effects have been shown to be sufficient to utilise this capability.

(*c*) In over-tailored operation, the generation of a reflected shock instead of an unsteady expansion between the region *sd*2/3 interface will result in reduced performance compared to operation without a secondary driver.

(*d*) Figure 7 shows the density ratio ρ_{sd1}/ρ_1 below which a reflected shock will arise, based on an ideal gas analysis; in the limiting case, $\rho_{sd1}/\rho_1 < 1$ will produce a reflected shock and therefore a performance drop. For (relatively) heavy test gases such as air, this proves to be a restrictive condition which effectively limits the secondary driver as a performance-increasing device to superorbital conditions only, since the test gas (air) must initially be at a lower density than the secondary driver (helium). However, this is less restrictive when lighter test gases are used (for example, Gas Giant flows comprised primarily of helium and hydrogen, which can have order-of-magnitude lower molecular masses).

(*e*) Morgan & Stalker (1991) identified an additional use for the secondary driver: in over-tailored operation it can theoretically provide the necessary acoustic buffer (Paull & Stalker 1992) to prevent ingress of driver-induced flow disturbances to the test gas, where such a buffer would not exist with the primary driver alone. Figure 17 shows the practical implementation of this principle for a theoretical scramjet Mach 10 condition. Operation with and without a secondary driver was experimentally examined for a Mach 14 flow condition; it was found that (i) acceleration tube shock speeds were consistently lower when using a secondary driver, even though shock tube shock speeds were more closely matched; (ii) cone impact pressure measurements indicated a period of approximately constant

pressure without a secondary driver, but were constantly rising during the test time (with no apparent steady region) with a secondary driver; results from the larger X3 facility indicate a less severe pressure gradient, therefore it does not necessarily appear to be intrinsic to the secondary driver; (iii) high-frequency noise appeared to be significantly reduced when the secondary driver was used, so long as it was over-tailored.

(*f*) Considering the secondary driver as an acoustic buffer, this study has demonstrated that most practical flow conditions which would benefit from this arrangement will have a strong reflected shock through the secondary driver gas. It has been shown in this paper that this reflected shock reflects from the *sd*3/*sd*2 region interface, resulting in a subsequent upstream running compression wave. For most practical arrangements, this compression wave will arrive at the test gas long before the test gas reaches the test section, and its effect on test gas acoustics needs to be assessed.

(*g*) This upstream running compression wave invalidates 0-D theoretical estimates of the flow in this operating mode, since the wave processes become strongly coupled. In simple terms, the helium secondary driver gas becomes a passive intermediate gas slug which is compressed between the expanded driver gas and shock-processed test gas. It ceases to significantly influence the bulk test flow properties, which instead approach the equivalent properties for operation without a secondary driver, albeit those for a shorter tube.

(*h*) The ideal gas theoretical analysis of §3 demonstrated the same qualitative trends as the specific performance analysis of X2 using equilibrium chemistry in §§4–7. This provides confidence that the observations from the X2 study will be applicable to expansion tubes generally.

Future efforts need to address the following remaining questions:

(*a*) For the low-enthalpy case, where the secondary driver is processed by a reflected shock, whether or not the secondary driver remains effective as an acoustic buffer in accordance with the original analysis by Paull & Stalker (1992).

(*b*) For configurations where the secondary driver is over-tailored in relation to the primary driver gas, the test gas (region 2) may still be under-tailored in relation to the shock-processed secondary driver gas (region *sd*2); in such cases, it is necessary to establish what amount of noise is present in the secondary driver gas due to secondary diaphragm rupture and passage down the tube, and whether or not this noise transmits to the test gas and degrades the test flow quality.

(*c*) Determine if there is an ideal ratio of over-tailoring of the secondary driver gas, and under-tailoring of the test gas, that leads to an optimal test flow.

9. Conclusion

This paper has provided an overview of results from a study of expansion tube operation with a secondary driver. Facility performance across the entire practical operating envelope of the X2 facility has been assessed. It has been shown that operating characteristics can vary significantly, and depend primarily on the initial density ratio between the secondary driver gas and test gas. When the secondary driver gas is denser than the test gas, it undergoes an unsteady expansion into the test gas, and a theoretical performance increase can be achieved. When the test gas is denser, the secondary driver gas is instead processed by a reflected shock, which becomes coupled to primary driver wave processes. This complicates local flow processes, and subsequently invalidates traditional analytical performance estimates.

Acknowledgements

Appendix A. Analytical solution procedure for prediction of expansion tube flow processes

A.1. *Basic free-piston driver with area change*

This appendix considers a free-piston-driven shock tube with driver area change. Referring to figure 1, and assuming that the following quantities are initially specified:

(i) $T_{4,i}$ and T_1; initial temperatures of driver gas and test gas;
(ii) λ; compression ratio of driver gas after free-piston compression;
(iii) p_4/p_1; ratio between driver gas and test gas pressures at moment of diaphragm rupture;
(iv) γ_4 and γ_1; driver and test gas specific heat ratios;
(v) R_4 and R_1; driver and test gas specific gas constants.

The driver gas is compressively heated from its initial fill temperature, $T_{4,i}$, to its temperature at rupture, T_4:

$$T_4 = T_{4,i}\lambda^{\gamma_4-1}. \tag{A 1}$$

When the diaphragm ruptures, the initially stagnant driver gas ($T_4 = T_{4,0}$) begins to expand into the driven tube. An unsteady expansion processes the driver gas from region 4 to region 4′. For large area reductions from the driver to driven tubes, it is reasonable to assume that there are negligible total pressure and temperature losses through this subsonic driver gas expansion (Morgan 2001*b*):

$$T_4 = T_{4,0} \approx T_{4'} \approx T_{4',0}. \tag{A 2}$$

A steady expansion then processes the driver gas to state 4″ across the area change. The Mach number is 1.0 since the flow is choked:

$$Ma_{4''} = 1.0. \tag{A 3}$$

Stagnation and static properties are related as follows through the steady expansion:

$$\frac{T_{4'',0}}{T_{4''}} = 1 + \frac{\gamma_4 - 1}{2}Ma_{4''}^2. \tag{A 4}$$

The total temperature and pressure remain constant through the steady expansion; substituting $T_{4'',0} = T_{4',0}$, equations (A 2) and (A 3) into (A 4):

$$T_{4''} = \frac{2T_4}{\gamma_4 + 1}. \tag{A 5}$$

The velocity across the area change is as follows:

$$u_{4''} = a_{4''} = \sqrt{\gamma_4 R_4 T_{4''}}. \tag{A 6}$$

Assuming isentropic flow from regions 4 to 4″:

$$\frac{p_{4''}}{p_4} = \left(\frac{T_{4''}}{T_4}\right)^{\gamma_4/(\gamma_4-1)}. \tag{A 7}$$

Across the unsteady expansion between regions $4''$ and 3, velocity and sound speed are related as follows:

$$u_3 + \frac{2a_3}{\gamma_3 - 1} = u_{4''} + \frac{2a_{4''}}{\gamma_4 - 1}. \quad (A\,8)$$

Noting (A 6), that $\gamma_3 = \gamma_4$, substituting these into (A 8) and rearranging:

$$u_3 = \frac{a_{4''}(\gamma_4 + 1) - 2a_3}{\gamma_4 - 1} = \frac{\sqrt{\gamma_4 R_4}}{\gamma_4 - 1}[\sqrt{T_{4''}}(\gamma_4 + 1) - 2\sqrt{T_3}]. \quad (A\,9)$$

The induced flow velocity behind the shock in region 2, u_2, is given by standard shock relations:

$$u_2 = \frac{a_1}{\gamma_1}\left(\frac{p_2}{p_1} - 1\right)\left[\frac{\dfrac{2\gamma_1}{\gamma_1 + 1}}{\dfrac{p_2}{p_1} + \dfrac{\gamma_1 - 1}{\gamma_1 + 1}}\right]^{1/2}. \quad (A\,10)$$

The pressure in region 3 is equal to region 2, i.e. $p_3 = p_2$, therefore temperature in region 3 can be calculated from isentropic relations:

$$\frac{p_3}{p_{4''}} = \frac{p_2}{p_{4''}} = \frac{p_2}{p_4} \cdot \frac{p_4}{p_{4''}} = \frac{p_2}{p_1} \cdot \frac{p_1}{p_4} \cdot \frac{p_4}{p_{4''}}, \quad (A\,11)$$

$$T_3 = T_{4''}\left(\frac{p_3}{p_{4''}}\right)^{(\gamma_4 - 1)/\gamma_4} = T_{4''}\left(\frac{p_2}{p_1} \cdot \frac{p_1}{p_4} \cdot \frac{p_4}{p_{4''}}\right)^{(\gamma_4 - 1)/\gamma_4}. \quad (A\,12)$$

Substituting (A 12) into (A 9) and noting that $u_2 = u_3$ across the interface:

$$\frac{a_1}{\gamma_1}\left(\frac{p_2}{p_1} - 1\right)\left[\frac{\dfrac{2\gamma_1}{\gamma_1 + 1}}{\dfrac{p_2}{p_1} + \dfrac{\gamma_1 - 1}{\gamma_1 + 1}}\right]^{1/2} = \frac{\sqrt{\gamma_4 R_4 T_{4''}}}{\gamma_4 - 1}\left[\gamma_4 + 1 - 2\left(\frac{p_2}{p_1} \cdot \frac{p_1}{p_4} \cdot \frac{p_4}{p_{4''}}\right)^{(\gamma_4 - 1)/2\gamma_4}\right].$$

$$(A\,13)$$

After evaluating (A 1), (A 5) and (A 7), (A 13) can be used to solve for the resulting shock pressure ratio p_2/p_1.

A.2. *Compound driver with area change*

A free-piston-driven shock tube, with a secondary driver between the primary diaphragm and shock tube, is now considered. Referring to either figure 3 or 5, the configuration parameters are the same as in §A.1, except the following initial quantities must additionally be specified:

(i) T_{sd1}; initial temperature in secondary driver;
(ii) p_{sd1}/p_1; initial ratio of secondary driver and test gas pressure ratios;
(iii) γ_{sd}; secondary driver ratio of specific heats;
(iv) R_{sd}; secondary driver specific gas constant.

The shock speed through the secondary driver can be calculated by solving (A 15) for the ratio p_{sd2}/p_{sd1}; this equation is simply an adaptation of (A 13), with the additional substitution shown in (A 14):
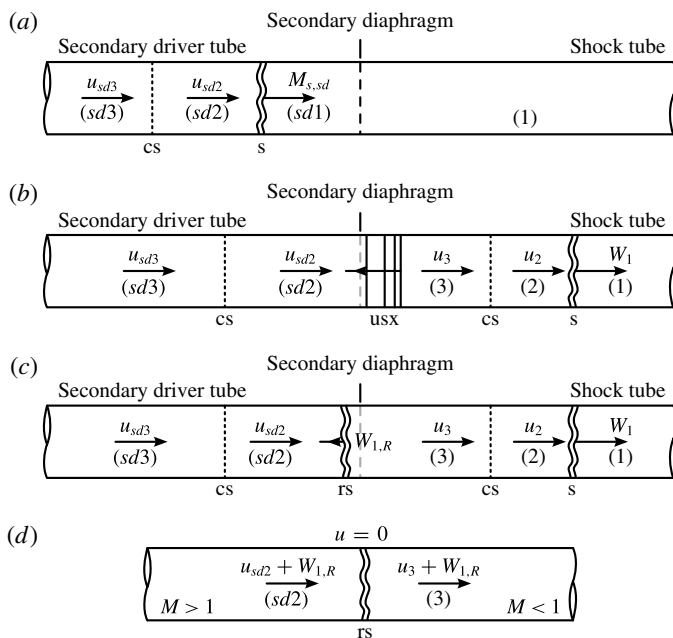
FIGURE 20. Reflected shock and unsteady expansion solutions following secondary diaphragm rupture: (*a*) prior to shock arrival at secondary diaphragm; (*b*) after diaphragm rupture; $u_3 > u_{sd2}$ and $p_3 < p_{sd2}$; (*c*) after diaphragm rupture; $u_3 < u_{sd2}$ and $p_3 > p_{sd2}$; (*d*) reflected shock from (*c*) in shock steady coordinate system: s = shock; rs = reflected shock; cs = contact surface; usx = unsteady expansion.

$$\frac{p_{sd1}}{p_4} = \frac{p_{sd1}}{p_1} \cdot \frac{p_1}{p_4}, \tag{A 14}$$

$$\frac{a_{sd1}}{\gamma_{sd}} \left(\frac{p_{sd2}}{p_{sd1}} - 1\right) \left[\frac{\dfrac{2\gamma_{sd}}{\gamma_{sd} + 1}}{\dfrac{p_{sd2}}{p_{sd1}} + \dfrac{\gamma_{sd} - 1}{\gamma_{sd} + 1}}\right]^{1/2}$$

$$= \frac{\sqrt{\gamma_4 R_4 T_{4''}}}{\gamma_4 - 1} \left[\gamma_4 + 1 - 2\left(\frac{p_{sd2}}{p_{sd1}} \cdot \frac{p_{sd1}}{p_1} \cdot \frac{p_1}{p_4} \cdot \frac{p_4}{p_{4''}}\right)^{(\gamma_4 - 1)/2\gamma_4}\right]. \tag{A 15}$$

Referring to figure 20, either an unsteady expansion (figure 20*b*) or a reflected shock (figure 20*c*) may process the region *sd*2 gas. Initially, an unsteady expansion will be assumed to occur; if the solution predicts a pressure drop from regions p_{sd2} to p_3, then the assumption will be considered valid. Otherwise, if $p_{sd2} < p_3$, the assumption will be considered invalid, and the calculation must be repeated assuming a reflected shock.

A.2.1. *Unsteady expansion at secondary diaphragm*

Referring to figure 20(*b*), an unsteady expansion transforms the secondary driver gas from state *sd*2 to state 3. Equation (A 16) relates the flow properties across the

unsteady expansion:

$$u_3 + \frac{2a_3}{\gamma_3 - 1} = u_{sd2} + \frac{2a_{sd2}}{\gamma_{sd} - 1}. \tag{A 16}$$

u_{sd2} and T_{sd2} are given by (A 17) and (A 18), respectively, and can be calculated once (A 15) has been solved:

$$u_{sd2} = \frac{a_{sd1}}{\gamma_{sd}} \left(\frac{p_{sd2}}{p_{sd1}} - 1 \right) \left[\frac{\frac{2\gamma_{sd}}{\gamma_{sd} + 1}}{\frac{p_{sd2}}{p_{sd1}} + \frac{\gamma_{sd} - 1}{\gamma_{sd} + 1}} \right]^{1/2}, \tag{A 17}$$

$$T_{sd2} = T_{sd1} \frac{p_{sd2}}{p_{sd1}} \left(\frac{\frac{\gamma_{sd} + 1}{\gamma_{sd} - 1} + \frac{p_{sd2}}{p_{sd1}}}{1 + \frac{\gamma_{sd} + 1}{\gamma_{sd} - 1} \cdot \frac{p_{sd2}}{p_{sd1}}} \right). \tag{A 18}$$

Expanding sound speed terms in (A 16), noting that $\gamma_3 = \gamma_{sd}$, and solving for u_3:

$$u_3 = u_{sd2} + \frac{2\sqrt{\gamma_{sd} R_{sd}}}{\gamma_{sd} - 1} (\sqrt{T_{sd2}} - \sqrt{T_3}). \tag{A 19}$$

T_3 is related to T_{sd2} by isentropic relations:

$$T_3 = T_{sd2} \left(\frac{p_3}{p_{sd2}} \right)^{(\gamma_{sd} - 1)/\gamma_{sd}}. \tag{A 20}$$

Expanding (A 20) and noting that $p_2 = p_3$:

$$T_3 = T_{sd2} \left(\frac{p_2}{p_1} \cdot \frac{p_1}{p_{sd1}} \cdot \frac{p_{sd1}}{p_{sd2}} \right)^{(\gamma_{sd} - 1)/\gamma_{sd}}. \tag{A 21}$$

Substituting (A 21) into (A 19) and noting that $u_3 = u_2$ (which was already provided in (A 10)):

$$\frac{a_1}{\gamma_1} \left(\frac{p_2}{p_1} - 1 \right) \left[\frac{\frac{2\gamma_1}{\gamma_1 + 1}}{\frac{p_2}{p_1} + \frac{\gamma_1 - 1}{\gamma_1 + 1}} \right]^{1/2}$$
$$= u_{sd2} + \frac{2\sqrt{\gamma_{sd} R_{sd} T_{sd2}}}{\gamma_{sd} - 1} \left[1 - \left(\frac{p_2}{p_1} \cdot \frac{p_1}{p_{sd1}} \cdot \frac{p_{sd1}}{p_{sd2}} \right)^{(\gamma_{sd} - 1)/2\gamma_{sd}} \right]. \tag{A 22}$$

Equation (A 22) can be used to solve for the pressure ratio p_2/p_1. The solution will be valid for $p_3/p_{sd2} < 1$; this ratio can be evaluated using (A 23):

$$\frac{p_3}{p_{sd2}} = \frac{p_2}{p_{sd2}} = \frac{p_2}{p_1} \cdot \frac{p_1}{p_{sd1}} \cdot \frac{p_{sd1}}{p_{sd2}}. \tag{A 23}$$

If $p_3/p_{sd2} > 1$, the shock-processed secondary driver gas is processed by a reflected shock at the secondary diaphragm, and the reflected shock solution must be evaluated.

A.2.2. *Reflected shock at secondary diaphragm*

Referring to figure 5, the shock-processed secondary driver gas (region *sd*2) decelerates and is compressed after it impacts the relatively dense test gas (region 1); this occurs through a reflected shock. Although the shock may travel from left to right in the laboratory reference system, in the shock steady coordinate system it travels from right to left into the region *sd*2 flow, as shown in figure 20(*d*). Let W be the velocity of the gas ahead of the shock wave, and $(W - u_p)$ be the velocity of the induced mass flow behind the shock wave, both relative to the shock wave:

$$W = u_{sd2} + W_{1,R} \rightarrow W_{1,R} = W - u_{sd2}, \tag{A 24}$$

$$W - u_p = u_3 + W_{1,R} \rightarrow W_{1,R} = W - u_p - u_3. \tag{A 25}$$

Equating (A 24) and (A 25):

$$W - u_{sd2} = W - u_p - u_3 \rightarrow u_p = u_{sd2} - u_3. \tag{A 26}$$

The induced flow velocity behind the reflected shock is given by:

$$u_p = \frac{a_{sd2}}{\gamma_{sd}} \left(\frac{p_3}{p_{sd2}} - 1 \right) \left(\frac{\dfrac{2\gamma_{sd}}{\gamma_{sd} + 1}}{\dfrac{p_3}{p_{sd2}} + \dfrac{\gamma_{sd} - 1}{\gamma_{sd} + 1}} \right)^{1/2}. \tag{A 27}$$

Equating (A 26) and (A 27), noting that $u_3 = u_2$ (provided in (A 10)), and making the (A 23) substitution:

$$u_{sd2} - \frac{a_1}{\gamma_1} \left(\frac{p_2}{p_1} - 1 \right) \left(\frac{\dfrac{2\gamma_1}{\gamma_1 + 1}}{\dfrac{p_2}{p_1} + \dfrac{\gamma_1 - 1}{\gamma_1 + 1}} \right)^{1/2}$$

$$= \frac{a_{sd2}}{\gamma_{sd}} \left(\frac{p_2}{p_1} \cdot \frac{p_1}{p_{sd1}} \cdot \frac{p_{sd1}}{p_{sd2}} - 1 \right) \left(\frac{\dfrac{2\gamma_{sd}}{\gamma_{sd} + 1}}{\dfrac{p_2}{p_1} \cdot \dfrac{p_1}{p_{sd1}} \cdot \dfrac{p_{sd1}}{p_{sd2}} + \dfrac{\gamma_{sd} - 1}{\gamma_{sd} + 1}} \right)^{1/2}. \tag{A 28}$$

Solution of (A 28) will yield the test gas pressure ratio, p_2/p_1, for the reflected shock case. This solution is valid for $p_3/p_{sd2} > 1$; this ratio can be evaluated with (A 23).

A.3. *Reflected Mach wave at the secondary diaphragm*

Referring to §A.2, the secondary driver gas is processed by either an unsteady expansion or a reflected shock wave after the secondary diaphragm is ruptured. In this section the density ratio associated with the transition from an unsteady expansion to a reflected shock is derived. Considering the case of the weakest possible reflected shock – the Mach wave – there will be no pressure rise across the shock, therefore the ratio $p_3/p_{sd2} = 1$, and there is no induced mass flow velocity behind the shock. Substituting $p_3 = p_2 = p_{sd2}$ and u_{sd2} from (A 17) into (A 28):

$$\frac{a_{sd1}}{\gamma_{sd}} \left(\frac{p_{sd2}}{p_{sd1}} - 1 \right) \left[\frac{\dfrac{2\gamma_{sd}}{\gamma_{sd} + 1}}{\dfrac{p_{sd2}}{p_{sd1}} + \dfrac{\gamma_{sd} - 1}{\gamma_{sd} + 1}} \right]^{1/2} - \frac{a_1}{\gamma_1} \left(\frac{p_2}{p_1} - 1 \right) \left(\frac{\dfrac{2\gamma_1}{\gamma_1 + 1}}{\dfrac{p_2}{p_1} + \dfrac{\gamma_1 - 1}{\gamma_1 + 1}} \right)^{1/2} = 0. \tag{A 29}$$

Equation (A 29) applies for the case of an infinitely weak reflected shock at the secondary diaphragm. The pressure ratio across the secondary driver shock, p_{sd2}/p_{sd1}, can be solved in terms of the pressure ratio across the shock through the test gas, p_2/p_1. The following substitutions are made:

$$\left(\frac{p_{sd2}}{p_{sd1}}\right)_r = \text{reflected Mach wave pressure ratio}, \tag{A 30}$$

$$\varrho = \left(\frac{p_{sd2}}{p_{sd1}}\right)_r - 1, \tag{A 31}$$

$$\kappa_1 = \frac{2\gamma_{sd}}{\gamma_{sd}+1}, \tag{A 32}$$

$$\kappa_2 = \frac{\gamma_{sd}}{a_{sd1}} \frac{a_1}{\gamma_1} \left(\frac{p_2}{p_1}-1\right) \left(\frac{\dfrac{2\gamma_1}{\gamma_1+1}}{\dfrac{p_2}{p_1}+\dfrac{\gamma_1-1}{\gamma_1+1}}\right)^{1/2}. \tag{A 33}$$

Substituting (A 31)–(A 33) into (A 29) and rearranging:

$$\varrho^2 + \left(-\frac{\kappa_2^2}{\kappa_1}\right)\varrho + (-\kappa_2^2) = 0, \tag{A 34}$$

which can be solved using the quadratic formula:

$$\varrho = \frac{\kappa_2^2/\kappa_1 \pm \sqrt{\kappa_2^4/\kappa_1^2 + 4\kappa_2^2}}{2}. \tag{A 35}$$

Substituting (A 31) into (A 35):

$$\left(\frac{p_{sd2}}{p_{sd1}}\right)_r = \frac{\kappa_2^2/\kappa_1 \pm \sqrt{\kappa_2^4/\kappa_1^2 + 4\kappa_2^2}}{2} + 1. \tag{A 36}$$

Noting that this solution only applies to the reflected Mach wave case, $p_2 = p_3 = (p_{sd2})_r$:

$$\frac{(p_{sd1})_r}{p_1} = \left(\frac{p_{sd1}}{p_{sd2}}\right)_r \frac{(p_{sd2})_r}{p_2} \frac{p_2}{p_1} = \left(\frac{p_{sd1}}{p_{sd2}}\right)_r \cdot 1 \cdot \frac{p_2}{p_1} = \left(\frac{p_{sd1}}{p_{sd2}}\right)_r \frac{p_2}{p_1}. \tag{A 37}$$

Equation (A 37) can be used to determine the ratio between secondary driver and shock tube fill pressures which will produce a reflected Mach wave in the secondary driver gas. For $p_{sd1}/p_1 \leqslant (p_{sd1})_r/p_1$, there will be a reflected shock wave into the secondary driver; for $p_{sd1}/p_1 \geqslant (p_{sd1})_r/p_1$, there will instead be an unsteady expansion of the region $sd2$ secondary driver gas. Equation (A 37) can be expressed in terms of an initial density ratio, assuming both gases initially have the same temperature:

$$\frac{(\rho_{sd1})_r}{\rho_1} = \left(\frac{p_{sd1}}{p_{sd2}}\right)_r \frac{p_2}{p_1} \frac{R_1}{R_{sd}}. \tag{A 38}$$

Equation (A 38) is plotted in figure 7, and the results are discussed in § 3.1.

REFERENCES

ANDERSON, J. D. JR. 1990 *Modern Compressible Flow with Historical Perspective*. McGraw-Hill, International Edition.

ANDERSON, J. D. JR. 2006 *Hypersonic and High-Temperature Gas Dynamics*, 2nd edn. AIAA Education Series.

ANDERSON, G., KUMAR, A. & ERDOS, J. 1990 Progress in hypersonic combustion technology with computation and experiment. In *Proceedings of the Second International Aerospace Planes Conference, Orlando, FL, October 29–31*.

BAKOS, R. J. & ERDOS, J. I. 1995 Options for enhancement of the performance of shock-expansion tubes and tunnels. In *Proceedings of the 33rd Aerospace Sciences Meeting and Exhibit, Reno, NV, January 9–12*.

BAKOS, R. J., MORGAN, R. G. & TAMAGNO, J. 1992 Effects of oxygen dissociation on hypervelocity combustion experiments. In *Proceedings of the AIAA 17th Aerospace Ground Testing Conference, Nashville, TN, July 6–8*.

BILLIG, F. 1993 Research on supersonic combustion. *J. Propul. Power* **9** (4), 499–514.

CAPRA, B. R. & MORGAN, R. G. 2012 Radiative and total heat transfer measurements to a Titan explorer model. *J. Spacecr. Rockets* **49** (1), 12–23.

CHINITZ, W., ERDOS, J., RIZKALLA, O., ANDERSON, G. & BUSHNELL, D. 1994 Facility opportunities and associated stream chemistry considerations for hypersonic air-breathing propulsion. *J. Propul. Power* **10** (1), 6–17.

COESA (1976) U.S. Standard Atmosphere 1976, National Oceanic and Atmospheric Administration, National Aeronautics and Space Administration, United States Air Force, *Tech. Rep.* U.S. Government Printing Office, Washington, DC.

CURRAN, E. 2001 Scramjet engines: the first forty years. *J. Propul. Power* **17** (6), 1138–1148.

DUFF, R. E. 1959 Shock-tube performance at low initial pressure. *Phys. Fluids* **2** (2), 207–216.

EICHMANN, T. N. 2012 Radiation measurements in a simulated Mars atmosphere. PhD thesis, School of Mathematics & Physics, The University of Queensland, Brisbane, Australia.

GILDFIND, D. E. 2012 Development of high total pressure scramjet flow conditions using the X2 expansion tube. PhD thesis, School of Mechanical and Mining Engineering, The University of Queensland, Brisbane.

GILDFIND, D. E., JAMES, C. M. & MORGAN, R. G. 2015 Free-piston driver performance characterisation using experimental shock speeds through helium. *Shock Waves* **25** (2), 169–176.

GILDFIND, D. E., MORGAN, R. G., MCGILVRAY, M. & JACOBS, P. A. 2014 Production of high-Mach-number scramjet flow conditions in an expansion tube. *AIAA J.* **52** (1), 162–177.

GILDFIND, D. E., MORGAN, R. G., MCGILVRAY, M., JACOBS, P. A., STALKER, R. J. & EICHMANN, T. N. 2011 Free-piston driver optimisation for simulation of high Mach number scramjet flow conditions. *Shock Waves* **21** (6), 559–572.

GILDFIND, D. E., SANCHO, J. & MORGAN, R. G. 2013 High Mach number scramjet test flows in the X3 expansion tube. In *Proceedings of the 29th International Symposium on Shock Waves, University of Wisconsin–Madison, Memorial Union, July 14–19*.

GORDON, S. & MCBRIDE, B. J. 1994 Computer program for calculation of complex chemical equilibrium compositions and applications. *NASA Tech. Rep.* RP-1311, Cleveland, OH.

HENSHALL, B. 1956 The use of multiple diaphragms in shock tubes. *ARC Tech. Rep.* C.P. No. 291.

HICKS, J. 1993 Flight testing of airbreathing hypersonic vehicles. *NASA Tech. Rep.* TM-4524, Dryden Flight Research Facility, Edwards, California.

HUNT, J. & MARTIN, J. 2000 Rudiments and methodology for design and analysis of hypersonic air-breathing vehicles. In *Scramjet Propulsion*, Progress in Astronautics and Aeronautics, vol. 189, chap. 15, pp. 939–978. AIAA.

JACOBS, P. A. 1994 Numerical simulation of transient hypervelocity flow in an expansion tube. *Comput. Fluids* **23** (1), 77–101.

JACOBS, P. A. 1994 Quasi-one-dimensional modeling of a free-piston shock tunnel. *AIAA J.* **32** (1), 137–145.

JACOBS, C. M. 2011 Radiation in low density hypervelocity flows. PhD thesis, School of Mechanical and Mining Engineering, The University of Queensland, Brisbane, Australia.

JAMES, C. J., GILDFIND, D. E., MORGAN, R. G. & MCINTYRE, T. J. 2014 The limits of simulating Gas Giant entry at true gas composition and true flight velocities in an expansion tube. In *Proceedings of the 19th Australasian Fluid Mechanics Conference, Melbourne, Australia, 8–11 December*.

JONES, J. J. 1965 Some performance characteristics of the LRC 3 3/4-inch pilot expansion tube using an unheated hydrogen driver. In *Proceedings of the Fourth Hypervelocity Techniques Symposium, Arnold Engineering Development Center, Arnold Air Force Station, Tennessee, 15–16 November* pp. 7–26.

KLICHE, D., MUNDT, C. & HIRSCHEL, E. H. 2011 The hypersonic Mach number independence principle in the case of viscous flow. *Shock Waves* **21**, 307–314.

LUCASIEWICZ, J. 1973 *Experimental Methods of Hypersonics*. Marcel Dekker.

MCGILVRAY, M., MORGAN, R. G. & JACOBS, P. A. 2010 Scramjet experiments in an expansion tunnel: evaluated using a quasi-steady analysis technique. *AIAA J.* **48** (8), 1635–1646.

MCINTYRE, T. J., LOUREL, I., EICHMANN, T. N., MORGAN, R. G., JACOBS, P. A. & BISHOP, A. I. 2001 An experimental expansion tube study of the flow over a toroidal ballute. *Tech. Rep.* Mechanical Engineering Research Report no. 2001/06, Centre for Hypersonics, The University of Queensland, November 15.

MILLER, C. G. 1977 Operational experience in the Langley expansion tube with various test gases. *NASA Tech. Rep.* TM 78637, NASA Langley Research Center, Hampton, VA, December.

MILLER, C. G. & JONES, J. J. 1983 Development and performance of the NASA Langley Research Center expansion tube/tunnel, a hypersonic-hypervelocity real-gas facility. In *Proceedings of the AIAA 14th International Symposium on Shock Waves, Sydney, Australia, Aug.* (ed. R. D. Archer & B. E. Milton), pp. 363–373.

MIRELS, H. 1963*a* Shock tube test time limitation due to turbulent-wall boundary layer. *AIAA J.* **2** (1), 84–93.

MIRELS, H. 1963*b* Test time in low-pressure shock tubes. *Phys. Fluids* **6** (9), 1201–1214.

MORGAN, R. G. 1997 Superorbital expansion tubes. In *Proceedings of the 21st International Symposium on Shock Waves, Great Keppel Island, Australia, July 20–25*.

MORGAN, R. G. 2001*a* Free-piston driven expansion tubes. In *Handbook of Shock Waves* (ed. G. Ben-Dor, O. Igra & T. Elperin), vol. 1, chap. 4.3, pp. 603–622. Elsevier.

MORGAN, R. G. 2001*b* Free-piston reflected shock tunnels. In *Handbook of Shock Waves* (ed. G. Ben-Dor, O. Igra & T. Elperin), vol. 1, chap. 4.2, pp. 587–601. Elsevier.

MORGAN, R. & STALKER, R. 1991 Double diaphragm driven free piston expansion tube. In *18th International Symposium on Shock Waves, July 21–26, Sendai, Japan*.

NASA 2010 Evaluation of the NASA Arc Jet capabilities to support mission requirements. *NASA Tech. Rep.* SP-577. Office of the Chief Engineer, 20110007355.

NEELY, A. J. & MORGAN, R. G. 1994 The superorbital expansion tube concept, experiment and analysis. *Aeronaut. J.* **98**, 97–105.

NORFLEET, G. D., LACEY, J. J. & WHITFIELD, J. D. 1965 Results of an experimental investigation of the performance characteristics of an expansion tube. In *Proceedings of the Fourth Hypervelocity Techniques Symposium, Arnold Engineering Development Center, Arnold Air Force Station, Tennessee, 15–16 November*, pp. 49–110.

OLDS, J. & BUDIANTO, I. 1998 Constant dynamic pressure trajectory simulation with POST. In *Proceedings of the 36th Aerospace Sciences Meeting and Exhibit, Jan. 12–15, Reno, NV, AIAA Paper* 1998-0302.

PAULL, A. & STALKER, R. 1992 Test flow disturbances in an expansion tube. *J. Fluid Mech.* **245**, 493–521.

PAULL, A., STALKER, R. J. & STRINGER, I. 1988 Experiments on an expansion tube with a free piston driver. In *Proceedings of the AIAA 15th Aerodynamic Testing Conference, San Diego, CA, 18–20 May, AIAA paper* 88-2018. AIAA; doi:10.2514/6.1988-2018.

PINCKNEY, S. Z. 1975 A short static-pressue probe design for supersonic flow. In *NASA Tech. Rep.* TN D-7978, Langley Research Center, Hampton, VA.

PORAT, H., ZANDER, F., MORGAN, R. G. & MCINTYRE, T. J. 2013 Emission spectroscopy of a Mach disk at Titan atmospheric entry conditions. In *Proceedings of the 29th International Symposium on Shock Waves, University of Wisconsin–Madison, Memorial Union, July 14–19*.

SHEIKH, U. A., JACOBS, C., LAUX, C. O., MORGAN, R. G. & MCINTYRE, T. J. 2013 Measurements of radiating flow fields in the vacuum ultraviolet. In *Proceedings of the 29th International Symposium on Shock Waves, University of Wisconsin–Madison, Memorial Union, July 14–19*.

SPURK, J. H. 1965 Design, operation, and preliminary results of the BLR expansion tube. In *Proceedings of the Fourth Hypervelocity Techniques Symposium, Arnold Engineering Development Center, Arnold Air Force Station, Tennessee, 15–16 Nov.*, pp. 111–144.

STALKER, R. J. 1990 Recent developments with free piston drivers. In *Current Topics in Shock Waves: 17th International Symposium on Shock Waves & Shock Tubes, Bethlehem, PA* (ed. Y. W. Kim), pp. 96–105. NASA.

STALKER, R. & PLUMB, D. 1968 Diaphragm-type shock tube for high shock speeds. *Nature* **218** (5143), 789–790.

STALKER, R. J. & PULSONETTI, M. 2004 Experiments on scaling of supersonic combustion. *Tech. Rep.* Research Report No. 2004/13, The University of Queensland, Brisbane.

STEWART, B. S., JACOBS, P. A. & MORGAN, R. G. 2001 The starting process of an expansion tube nozzle. In *Proceedings of the 23rd International Symposium on Shock Waves, The University of Texas at Arlington, USA, July 23–27*.

TRIMPI, R. L. 1962 A preliminary theoretical study of the expansion tube, a new device for producing high-enthalpy short-duration hypersonic gas flows. *NASA Tech. Rep.* R-133.